ABSTRACT

HANNA, BOTROS NASEIF. Evaluation of CFD Capability for Simulation of Energetic Flow in Light Water Reactor Containment. (Under the direction of Dr. Igor A. Bolotnov and Dr. Nam T. Dinh.)

This study is concerned with analysis of Direct Containment Heating (DCH), which is a known threat to the integrity of containment in Light Water Reactor plants during beyond design basis accident. DCH occurs in scenarios with high-pressure melt ejection (HPME) from the reactor vessel lower head to the containment. Molten corium release is followed by highly energetic steam flow, which causes melt dispersal and rapid heat up of the containment atmosphere. The present work investigates the capabilities of a computational fluid dynamics (CFD) approach for simulating high pressure steam blowdown. Evaluation Model Development and Assessment Process (EMDAP) is used to guide the investigation. Validation studies are conducted for selected flow patterns identified as important for the blowdown modeling. A three-dimensional mesh for the containment was designed and used to evaluate several turbulence models for their capability to capture key flow patterns under the reactor blowdown flow conditions.

Evaluation of CFD Capability for Simulation of Energetic Flow in Light Water Reactor
Containment

by
Botros Hanna

A thesis submitted to the Graduate Faculty of
North Carolina State University
in partial fulfillment of the
requirements for the degree of
Master of Science

Nuclear Engineering

Raleigh, North Carolina

2015

APPROVED BY:

_____   _____
Dr. Igor A. Bolotnov   Dr. Nam T. Dinh
Co-Chair   Co-Chair

_____   _____
Dr. Joseph M. Doster   Dr. Tiegang Fang

DEDICATION

To my parents.

BIOGRAPHY

The author graduated from Alexandria University, Egypt with a bachelor degree in nuclear engineering in 2010. He joined NCSU nuclear engineering department in 2012 and passed his PhD qualifying exam in 2013. Then, he started working with Dr. Igor A. Bolotnov and Dr. Nam T. Dinh in the fall of 2013. The author expects to continue his research after completing his master degree.

ACKNOWLEDGMENTS

TABLE OF CONTENTS

LIST OF TABLES

LIST OF FIGURES

NOMENCLATURE

Roman Symbols

d_p	Debris particles' diameter $[m]$
$M_{g,blow}$	Steam (gas) blowdown mass flow rate $[kg/s]$
$Q_{dep-gas}$	Energy produced from debris/steam interaction $[J/kg]$
ΔP	Pressure change $[Pa]$
P^0	Initial pressure $[Pa]$
U	Total internal energy $[J]$
V	Volume $[m^3]$
γ	Ratio of specific heats
E_b	Energy of reactor coolant system $[J]$
E_t	Latent heat of debris $[J]$
E_r	Metal oxidation energy $[J]$
E_{H_2}	Combustion of hydrogen energy $[J]$
E_w	Water vaporization energy $[J]$
u', v', w'	Velocity fluctuations in x, y, z directions $[m/s]$
K	Turbulent kinetic energy $[m^2/s^2]$
l_0	Integral length scale $[m]$
V_x, V_y, V_z	Time averaged velocity in x, y, z directions $[m/s]$
l_m	Mixing length $[m]$
y^+	Dimensionless distance to the wall
t	Time $[s]$
H	Jet-wall spacing $[m]$
D	Nozzle diameter $[m]$
M	Mach Number
I	Turbulence intensity
y	Height above impingement plate $[m]$
u_r	Radial velocity $[m/s]$
P_{rcs}^0	Initial pressure of reactor cooling system at blowdown $[Pa]$
T_{rcs}^0	Initial temperature of reactor cooling system at blowdown $[K]$
T_{UDW}^0	Initial Temperature of the Upper drywell $[K]$

T_{LDW}^0	Initial Temperature of the lower drywell $[K]$
a_0	Speed of sound [m/s]
m_0	Initial Discharge Rate at blowdown $[kg/s]$
A_{br}	Vessel breach area$[m^2]$
T_{conv}	Temperature at the convection area between UDW and LDW $[K]$
$\dot{m}_{conv}$	Mass flow rate through the convection area between UDW and LDW $[kg/s]$

Greek Symbols

τ	Characteristic time $[s]$
ψ	Ratio of heat capacities between fragmented debris and containment
H	Efficiency
ε	Energy dissipation rate$[m^2/s^3]$
ν	Kinematic viscosity $[m^2/s]$
H	Kolmogorov length scale [m]
u_η	Kolmogorov velocity scale [m/s]
τ_η	Kolmogorov time scale [s]
κ	Wave number [1/m]
μ_t	Turbulent viscosity $[Pa.s]$
ν_t	Turbulent kinematic viscosity $[m^2/s]$
ω	Turbulent specific dissipation rate $[1/s]$
τ_s	Time scale of discharge: blowdown time of steam [s]
η	Blowdown Discharge coefficient
ρ_s	Density of steam at RCS $[kg/m^3]$

Abbreviations

NRC	Nuclear Regulatory Commission
TMI	Three Mile Island
DCH	Direct Containment Heating
LOCA	Loss Of Coolant Accident

HPME	High Pressure Melt Ejection
CFD	Computational Fluid Dynamics
OpenFO	Open source Field Operation And Manipulation
SCE	Single Cell Equilibrium
TCE	Two Cell Equilibrium
CLCH	Convective Limited Containment Heating
AFDM	Advanced Fluid Dynamics Modeling
RANS	Reynolds Averaged Navier Stokes equations
RPV	Reactor Pressure Vessel

1 Introduction

1.1 Severe accidents in a light water reactor

Since the evolution of commercial nuclear power reactors, questions arose about the risk of nuclear power plants' accidents. In 1974, Atomic Energy Commission, the predecessor of the Department of Energy and the U.S. Nuclear Regulatory Commission (NRC) published a reactor safety study named WASH-1400, or Rasmussen report. This report predicted that the highest risk results from beyond design basis accidents, like a station blackout or containment bypass (radioactive materials' release to the environment). In 1979, Three Mile Island (TMI-2) accident reminded that severe accidents could occur. In 1986, Chernobyl accident showed a terrible impact of radioactive release when the reactor is destroyed in a plant without containment. Severe accident research accelerated after the TMI-2 and prompted again by the accident at Fukushima Daichi in March 2011. All these accidents showed that severe accidents may occur despite the continuous progress in nuclear safety procedures and measures. Therefore, it is essential for the nuclear industry to consider the severe accidents and their consequences during the design and licensing of the power plants.

Nuclear reactor accidents are qualified as severe when they include nuclear fuel melting. They occur with very low probability but could result in severe consequences. These accidents are usually caused by multiple failures in reactor cooling systems combined with subsequent failures in safety functions and/or human errors. A group of complex phenomena may occur depending on different scenarios, geometries and initial conditions. Figure 1.1 shows major phenomena that may occur during a severe accident in a Light Water Reactor. The presented work is a step to develop a novel approach to analyze one type of the severe accidents – the so-called Direct Containment Heating (DCH) [1, 2].

1.2 Direct containment heating

In the event of a prolonged station blackout to occur in a nuclear power plant in a loss of coolant accident (LOCA), the nuclear fuel reactor core can melt after a certain period of time if safety measures for core cooling are not taken timely. Consequently, molten corium relocates to the lower head of the reactor. Depending on the corium thermal load and the pressure in the vessel, the lower head may fail by thermal erosion or creep and corium flows down to the containment followed by high-pressure steam. If the reactor pressure boundaries, did not fail, the reactor system could retain a high pressure. In this scenario, upon failure of the reactor pressure vessel lower head, High Pressure Melt Ejection (HPME) may occur. The high-pressure steam blowdown leads to intensive mixing of corium and steam especially if the vessel failed at the bottom.

The melt is then atomized and dispersed by the blowdown steam. Heat exchange between the corium particles and the containment atmosphere will pressurize and heat up the containment. Oxidation of corium metals by steam results in hydrogen production. After mixing with oxygen, combustion can occur that also gives a pressure spike and heats the containment. Additionally, steam explosion may happen if the containment cavity is flooded. Because of all these dramatic consequences, HPME is given a special importance as it may produce highly undesirable events, such as early containment failure and early radioactive release from the nuclear plant to the environment [1, 2]. Figure 1.2 shows a simple diagram for direct containment heating scenario.
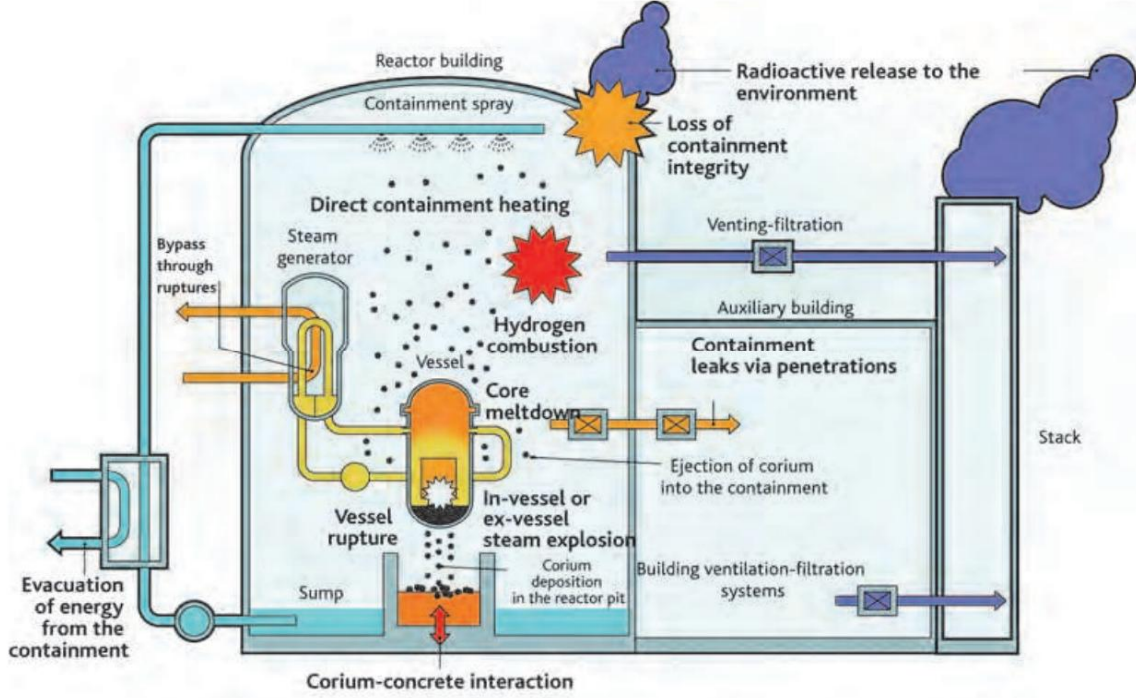
Figure 1.1: Major phenomena during a severe accident [2].

Figure 1.2 includes the main parameters: d_p, $M_{g,blow}$ τ_{ent}, τ_{set}, τ_{blow} and $Q_{dep-gas}$ which are corium debris particle diameter, steam (gas) blowdown mass flow rate, characteristic time for corium entrainment, characteristic time for particles' settling, characteristic time for steam blowdown and energy produced from the debris / steam interaction, respectively. The main physical processes that drive all these events are summarized in Figure 1.3 (see some snapshots for DCH simulation in Appendix A). In this work, steam blowdown, which is a phenomenon in DCH, is studied using Computational Fluid Dynamics (CFD) approach. We utilize open-source CFD package – OpenFOAM for this purpose.
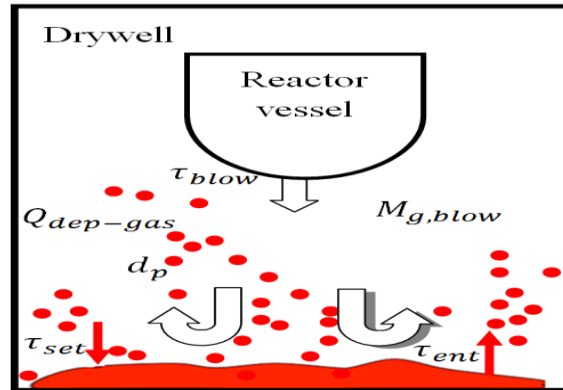
Figure 1.2: Simple diagram for Direct Containment Heating process: Corium ejection from the pressure vessel before steam blowdown [3].

Vessel failure and vessel hole ablation.

High Pressure Melt Ejection (HPME) to the containment.

Steam blowdown from reactor coolant system to containment.

Melt entrainment, atomization and dispersion.

Steam/melt thermal and chemical interactions.
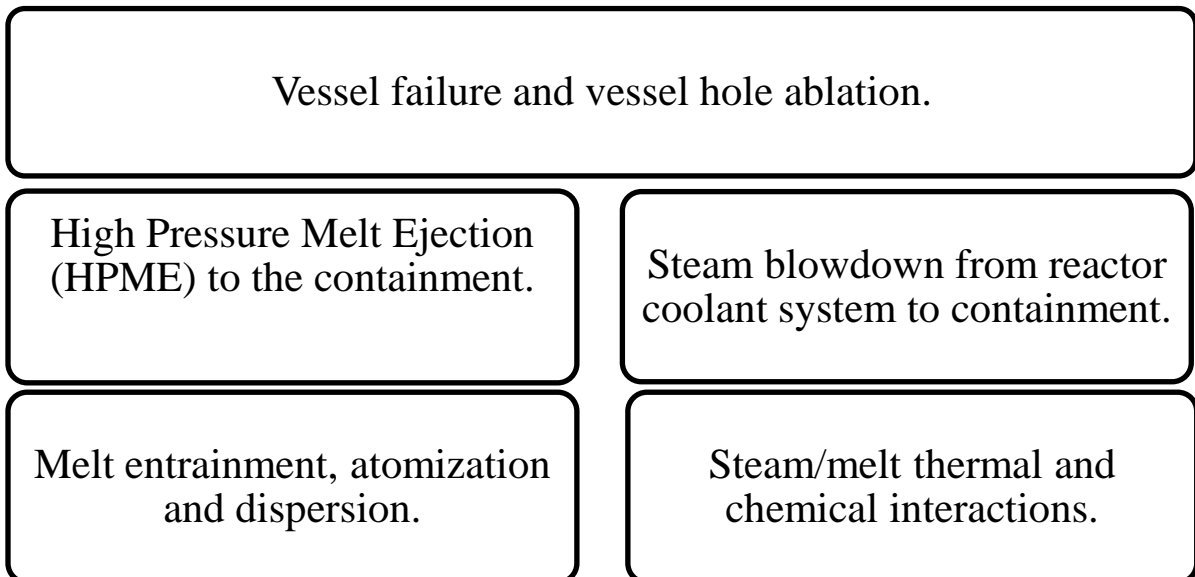
Figure 1.3: Key Physics in Direct Containment Heating [3]. Highlighted box refers to the focus of the thesis.

1.3 Computational fluid dynamics code – OpenFOAM

Modeling is essential to gain insights and identify sensitive parameters in any phenomena, and especially important for severe accident studies since limited experimental / real life observations are available. Three classes of models are used to investigate DCH: (i) simple analytical models; (ii) system level model and (iii) multidimensional models. CFD codes in particular are capable of providing very detailed (e.g. transient, three-dimensional) results compared to other approaches or experimental data for the problems under consideration. OpenFOAM (Open source Field Operation And Manipulation) is one of the available open-source CFD software packages [4]. Its object-oriented architecture allows the user to select any of its solvers depending on physics. The open source approach allows one to check the code or to modify it. It is based on C++ programming language with a structure that is shown in Figure 1.4 [4]. The capability of OpenFOAM for simulating steam blowdown is assessed in the presented research by validating its results against available experimental data.
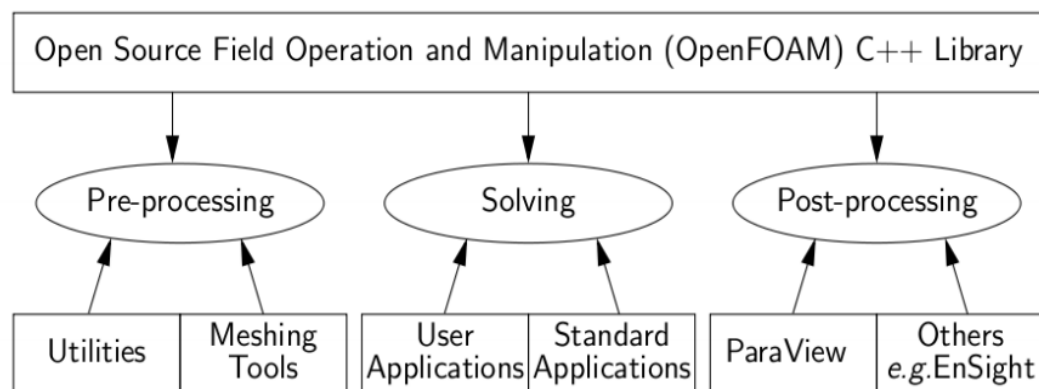
Figure 1.4: OpenFOAM Structure [4].

1.4   Verification and validation

Verification is necessary to ensure that the equations used by the numerical solver are correctly solved. Validation is important to evaluate the performance of our overall modeling approach for a given set of problems against the available experimental data [5]. This process allows us to evaluate how close a model represents the physical phenomena. In our case and in most practical cases (especially in the reactor accident analysis research area), it is hard to conduct a single experiment for the real system under the conditions of interest. Thus, we divide the modeling of the actual system into simpler sub-problems: (i) subsystem cases; (ii) benchmark cases and (iii) unit problems. Then, we compare simulation results with experimental data at various degrees of complexity. Subsystems usually represent 3 or more mixed types of physics. For benchmark cases, only 2 types of physics are considered. Unit problems represent the total decomposition of the complete system [5]. In the presented research, two benchmark cases are validated.

1.5   Thesis objectives and structure

In this work, CFD capability to simulate steam blowdown (as a part of the DCH scenario) is assessed. An attempt is made to contribute to CFD validation against key phenomena. In addition, we evaluate how to reduce the uncertainty related to turbulence modeling. Therefore the thesis is structured into 4 main components:

1. Literature review for Direct containment heating accident analysis methods and turbulence models mentioned in this work

2. Results of simulating the full scale system are presented and compared with lumped parameters' models

3. A systematic framework to evaluate OpenFOAM simulation capability through

- Identifying the focus, figure of merit and phenomena involved in steam blowdown phase

- Developing assessment base (through validation experiments).

- Performing assessment: Results from different available OpenFOAM solvers and turbulence models are compared.

- Simulating steam blowdown using three dimensional full scale mesh that represents the pressure vessel and containment.

4. Conclusion on perspectives of using CFD capabilities, turbulence models and the future work.

2 Literature review

To study DCH phenomena, researchers performed small scale experiments at different levels of detail [1]. These experiments provided insight into fluid dynamics of DCH as well as thermal and chemical interactions included in DCH. Typically, experiments cannot satisfy the full-scale conditions of the reactor and it is hard to do the experiment with the actual liquid (corium). Therefore, modeling tools are essential to gain better understanding of phenomena and to quantify the sensitivity of different parameters [1]. In this chapter, a summary of different modeling and simulation tools is presented (section 2.1). In the present research, Computational Fluid Dynamics (CFD) method is applied so we also discuss turbulence modeling as key issue in the CFD approach (see section 2.2).

2.1 Modeling and simulation of direct containment heating

In the past, research on Direct Containment Heating (DCH) has led to the development of different prediction methods. The simplest models are the analytical lumped parameter models, which can be applied without substantial computational expense (see subsection 2.1.1). The second category of models is the system codes, which are fully integrated and developed to simulate a spectrum of severe accidents (see subsection 2.1.2). The third category is the multidimensional CFD tools that are applied to simulate transient, multi-dimensional and multi-phase flow in reactor accident scenarios (see subsection 2.1.3).

2.1.1 Lumped parameter models

These models represent the major physics and key phenomena which lead to DCH serious consequences: containment pressurization, heat-up and hydrogen production. The initial analytical model is the adiabatic Single Cell Equilibrium (SCE) model [1, 6]. It

assumes that the entire containment is a single control volume and the corium fragmented debris is in equilibrium with the containment atmosphere. This model over-predicts the containment pressure rise as experiments had shown, thus it is deemed useful for calculating the upper limit of the containment pressure. The containment pressure change ΔP relative to the initial pressure P^0 is given by [1].

$$\frac{\Delta P}{P^0} = \frac{\Delta U}{U^0} = \frac{\sum \Delta E_i}{U^0 \, (1 + \psi)} \tag{2-1}$$

$$\Delta P = \frac{\gamma - 1}{V} \frac{(\Delta E_b + \Delta E_t + \Delta E_r + \Delta E_{H_2} + \Delta E_w)}{1 + \psi} \tag{2-2}$$

where U is the internal energy, V is the containment volume; γ is the ratio of specific heats; ψ is the ratio of heat capacity between fragmented debris and containment atmosphere; E_b is the energy of reactor coolant system (steam and water); E_t is the latent heat of debris, E_r is the metal oxidation. E_{H_2} is the combustion of hydrogen energy; E_w is the water vaporization energy.

Pressurization is over predicted because the model does not consider DCH mitigating processes like fragmented corium trapping in containment compartments as corium does not mix with the whole containment atmosphere. It also does not account for the corium liquid drop size and corium freezing.

The second model is the Two Cell Equilibrium Model (TCE) which accounts for the limitations of SCE by separating the thermal and chemical interactions into 2 locations: cavity plus compartment and the dome [1, 6]. Then, all processes are determined in two volumes as given by equations:

$$\Delta U = (\eta_1 + \eta_2)\Delta U_{singleCell} \tag{2-3}$$

$$\frac{\Delta P}{P^0} = (\eta_1 + \eta_2)\left[\frac{\Delta P}{P^0}\right]_{singleCell} \tag{2-4}$$

where the efficiencies η_1 and η_2 account for the individual contribution of each volume. Amount of steam interacting with corium is limited by the coherence ratio which is the ratio of the characteristic dispersal time to the characteristic time constant for steam blowdown. Debris dispersion is affected by the flow cross-section between the volumes. Energy deposition is also limited as equilibrium temperature is reached early in the smaller volume. Input correlations are needed for the fraction of melt ejected and the coherence time. TCE model was validated against experiments but it does not work if the cavity contains water [1].

CLCH model or the Convective Limited Containment Heating Model is a conceptual model that divides the containment into compartments and calculates the increase of pressure and temperature at different compartments after steam blowdown. It assumes Corium ejection from the bottom of the vessel (penetration) before steam blowdown so there is no coherence as Corium and steam are ejecting separately. The model equations are presented in Table 2.1 [3]. These equations are a little bit different from [3] because this work focuses on steam blowdown (this work does not account for Corium energy). Both CLCH and TCE were validated against specific experiments and they are restricted to geometries similar to the geometries of their relevant validation experiments.

2.1.2 System codes

System codes use control volume approach to perform affordable computation on a system level for severe accidents. They depend on validated correlations and analytical models. They do not serve help to understand different phenomena, but based on current level of knowledge. They also require tuning of several important parameters (like the heat transfer coefficient between droplets and containment atmosphere) to be used in various

conditions [1]. MELCOR is an example of integrated system code developed at Sandia National Laboratories for the U.S. Nuclear Regulatory Commission as a plant risk assessment tool. It is capable of modeling progression of accidents in light water reactor and nuclear power plants. It also estimates fission source term at these conditions and its sensitivity and uncertainty. For DCH, the dispersed corium debris is distributed into containment compartments. MELCOR simulates heat transfer to the atmosphere, chemical reaction and hydrogen combustion. The difficulty is selecting some time constants and input parameters which need experimental data for specific geometry [1, 7].

2.1.3   Multidimensional capability

Simulating DCH with CFD approach requires a three dimensional code with the multiphase flow simulation capability to represent different components (melt, solid debris, water, air and steam). One of the standard tools in industry for containment analyses is GOTHIC. GOTHIC is a multidimensional code which is typically used to model nuclear reactor containment buildings. It is a versatile software package for transient thermal hydraulic analysis of multiphase systems in complex geometries. It solves the mass, momentum and energy equations for multiphase flow. However, it uses a coarse mesh model so it cannot simulate all the aspects of the flow compared to CFD [8].

In addition, there is a two dimensional multiphase multi component code with special DCH models, called Advanced Fluid Dynamics Modeling (AFDM). It was validated against experiments at Sandia National Laboratory [9]. A recent trend is the application of commercial codes (e.g. OpenFOAM, ANSYS) to calculate separate processes such as steam blowdown [1].

2.2 Turbulence models

Some relevant points from the theory of turbulence are summarized in subsection 2.2.1. Turbulence modeling approaches are presented in subsection 2.2.2 with the focus on the Reynolds averaged Navier Stokes equation (RANS) modeling. This section gives a summary of turbulence modeling as explained in references [10, 11, 12, 13].

2.2.1 Some basic turbulent theory

Turbulence is a state of fluid motion which is characterized by the random nature of three dimensional motion. Turbulence can be considered as a dynamics set of eddies (vortices) of different sizes (scales). There are large scales where the energy enters the flow, the inertial range (intermediate scale) where energy flows to smaller scales of the dissipation range where the energy dissipates into heat. Eddies of the largest (integral) scale are characterized by a velocity on the order of the turbulent root mean square velocity fluctuations,

$$u' = (2k/3)^{1/2}$$
(2-5)

$$u' = (2k/3)^{1/2}$$
(2-6)

where k, the turbulent kinetic energy is defined as

$$k = \frac{1}{2}\langle u'_i u'_i \rangle = \frac{1}{2}\left(\overline{u'^2} + \overline{v'^2} + \overline{w'^2}\right)$$
(2-7)

where u', v', w' are the velocity fluctuations (or u'_1, u'_2, u'_3) in x, y, z directions. Integral length scale, l_0, is defined by

$$l_0 = \frac{k^{3/2}}{\varepsilon}$$
(2-8)

where ε $(\mathrm{m}^2/\mathrm{s}^3)$ is the energy dissipation rate [13].

Kolmogorov hypothesized that, at high Reynolds number, small eddies' statistics have a form that is determined by the energy dissipation rate, ε and kinematic viscosity, ν. Therefore Kolmogorov length scale (η), velocity scale (u_η) and time scale (τ_η) are defined as following

$$\eta = (\nu^3/\varepsilon)^{1/4}$$

(2-9)

$$u_\eta = (\varepsilon\nu)^{1/4}$$

(2-10)

$$\tau_\eta = (\nu/\varepsilon)^{1/2}$$

(2-11)

Table 2.1: CLCH model (for nomenclature, see page x) [3].

Vessel	$$\frac{P_{rcs}}{P_{rcs}^0} = \left(1 + \frac{\Gamma(\gamma-1)t}{2\tau_s}\right)^{\frac{-2\gamma}{\gamma-1}} \qquad (2\text{-}12)$$ $$M'_{g,blow} = m'_0 \left(1 + \frac{\Gamma(\gamma-1)t}{2\tau_s}\right)^{\frac{\gamma+1}{1-\gamma}} \qquad (2\text{-}13)$$ $$\frac{T_{rcs}}{T_{rcs}^0} = \left(\frac{P_{rcs}}{P_{rcs}^0}\right)^{(\gamma-1)/\gamma} \qquad (2\text{-}14)$$ $$\dot{m}_0 = \eta A_{br}\rho_s a_0 \gamma \qquad (2\text{-}15)$$ $$\Gamma = \left(\frac{2}{\gamma+1}\right)^{(\gamma+1)/2(\gamma-1)} \qquad (2\text{-}16)$$ $$\tau_s = \frac{V_{rcs}}{\eta a_0 A_b} \qquad (2\text{-}17)$$
LDW	$$\frac{d\left(m_{LDW}C_{v,LDW}T_{LDW}\right)}{dt} = M'_{g,blow}C_p^{H_2O}T_{rcs} - m_{conv}C_p^{H_2O}T_{conv} \qquad (2\text{-}18)$$ $$\frac{d(\dot{m}_{LDW})}{dt} = M'_{g,blow} - \dot{m}_{conv} \qquad (2\text{-}19)$$
UDW	$$\frac{d\left(m_{UDW}C_{v,UDW}T_{UDW}\right)}{dt} = \dot{m}_{conv}C_p^{H_2O}T_{conv} \qquad (2\text{-}20)$$ $$\frac{d(m_{UDW})}{dt} = \dot{m}_{conv} \qquad (2\text{-}21)$$

These scales correspond to the smallest motion of turbulence in a flow. Finally, to determine the turbulent kinetic energy distribution among the eddies of different size, energy spectrum $E(\kappa)$ is considered. $E(\kappa)$ is the energy contained in eddies of size l and wave

number $\kappa = 2\pi/l$. Figure 2.1 shows the energy distribution among energy containing range eddies, inertial range eddies and dissipation range eddies [13]. Navier-Stokes equations can be solved numerically to resolve all the spatial and temporal turbulence scales. However, this is not affordable for highly turbulent flows so turbulence modeling is necessary.

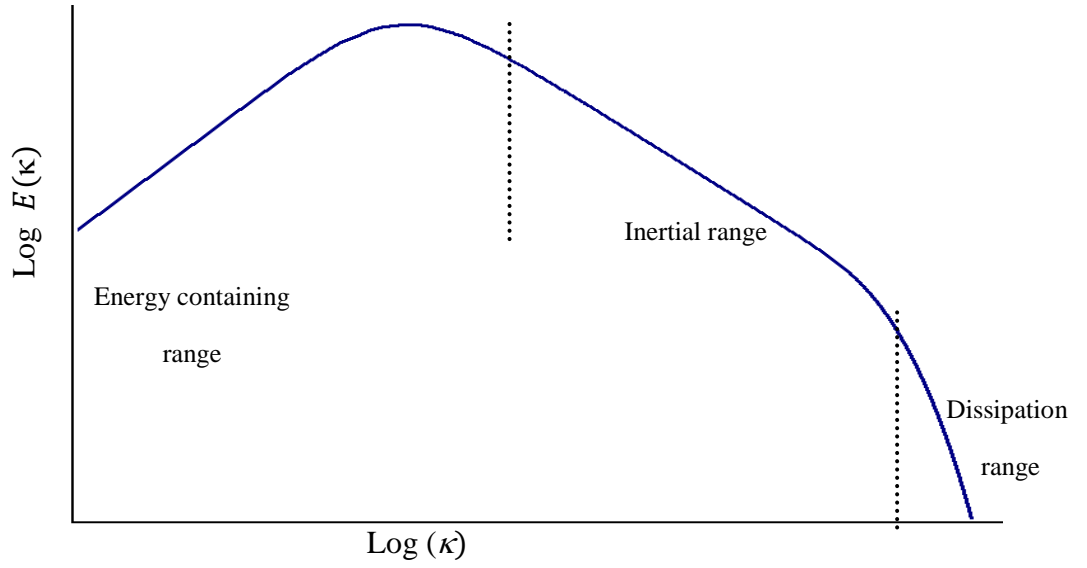**Figure 2.1: Distribution of turbulent energy in wave number space.**

2.2.2 Reynolds averaged Navier Stokes (RANS) modeling

RANS is the most common way to model turbulence in CFD. Reynolds decomposition of the velocity field into time averaged mean velocity component and turbulent fluctuating velocity component can be written as:

$$u = \overline{u} + u'$$

(2-22)

$$v = \overline{v} + v'$$

(2-23)

$$w = \overline{w} + w' \qquad (2\text{-}24)$$

The same decomposition was applied to other scalars (pressure and temperature). Time-averaging the Navier Stokes equations results in RANS equations

$$\frac{\partial \overline{u}}{\partial x} + \frac{\partial \overline{v}}{\partial y} + \frac{\partial \overline{w}}{\partial z} = 0 \qquad (2\text{-}25)$$

$$\rho \left(\frac{\partial \overline{u}}{\partial t} + \overline{u}\frac{\partial \overline{u}}{\partial x} + \overline{v}\frac{\partial \overline{u}}{\partial y} + \overline{w}_z \frac{\partial \overline{u}}{\partial z} \right)$$
$$= \frac{-\partial P}{\partial x} + \mu \left(\frac{\partial^2 \overline{u}}{\partial x^2} + \frac{\partial^2 \overline{u}}{\partial y^2} + \frac{\partial^2 \overline{u}}{\partial z^2} \right) - \rho \left(\frac{\overline{\partial u'u'}}{\partial x} + \frac{\overline{\partial u'v'}}{\partial y} + \frac{\overline{\partial u'w'}}{\partial z} \right) \qquad (2\text{-}26)$$

$$\rho \left(\frac{\partial \overline{v}}{\partial t} + \overline{u}\frac{\partial \overline{v}}{\partial x} + \overline{v}\frac{\partial \overline{v}}{\partial y} + \overline{w}\frac{\partial \overline{v}}{\partial z} \right)$$
$$= \frac{-\partial P}{\partial y} + \mu \left(\frac{\partial^2 \overline{v}}{\partial x^2} + \frac{\partial^2 \overline{v}}{\partial y^2} + \frac{\partial^2 \overline{v}}{\partial z^2} \right) - \rho \left(\frac{\overline{\partial v'u'}}{\partial x} + \frac{\overline{\partial v'v'}}{\partial y} + \frac{\overline{\partial v'w'}}{\partial z} \right) \qquad (2\text{-}27)$$

$$\rho \left(\frac{\partial \overline{w}}{\partial t} + \overline{u}\frac{\partial \overline{w}}{\partial x} + \overline{v}\frac{\partial \overline{w}}{\partial y} + \overline{w}\frac{\partial \overline{w}}{\partial z} \right)$$
$$= \frac{-\partial P}{\partial z} + \mu \left(\frac{\partial^2 \overline{w}}{\partial x^2} + \frac{\partial^2 \overline{w}}{\partial y^2} + \frac{\partial^2 \overline{w}}{\partial z^2} \right) - \rho \left(\frac{\overline{\partial w'u'}}{\partial x} + \frac{\overline{\partial w'v'}}{\partial y} + \frac{\overline{\partial w'w'}}{\partial z} \right) \qquad (2\text{-}28)$$

In RANS equations, last 3 terms on the right hand side (shown in red) are called Reynolds stresses. Noting that $\frac{\overline{\partial u'v'}}{\partial y} = \frac{\overline{\partial v'u'}}{\partial x}$, Reynolds stresses are 6 unknowns in addition to the other unknowns: $\overline{u}, \overline{v}, \overline{w}$ and P. There are 10 unknowns in 4 equations, so additional closure laws are needed to model the Reynolds stresses. Reynolds stresses are typically modeled according to Boussinesque eddy-viscosity approximation. Boussinesque assumed that Reynolds stresses are proportional to velocity gradients of the mean flow (similar to viscous stresses):

$$\rho \overline{u_i' u_j'} = \mu_t \left(\frac{\partial \overline{u_i}}{\partial x_j} + \frac{\partial \overline{u_j}}{\partial x_i} \right) - \frac{2}{3} \rho k \delta_{ij} \qquad \text{(2-29)}$$

$$\delta_{ij} = \begin{cases} 1, & i = j \\ 0, & i \neq j \end{cases} \qquad \text{(2-30)}$$

μ_t is the turbulent viscosity, an modeled quantity that serves as coefficient of proportionality between the mean flow velocity gradient and the Reynolds Stresses. The closure problem is to determine μ_t. A different approach is to make use of the second order models (Reynolds stresses) instead of Boussinesque hypothesis. The motivation for the second order models is to avoid the limitation related to turbulence isotropy (e.g. fitting 6 components with the same proportionality coefficient). However, these models include large number of partial differential equations which include many unknowns that require extra correlations [11]. To achieve reasonable simulation cost, the second order turbulence models were excluded from consideration in this research.

2.2.2.1   Zero-equation models

In these models, there are no partial differential equations present to obtain the closure relations. Algebraic relation is typically used to determine the eddy (turbulent) viscosity. Mixing length is introduced which is defined as the length over which there is high interaction of vortices in a turbulent flow field and it is problem-specific. Dimensional analysis shows that turbulent kinematic viscosity dimensions (m^2/s) is equivalent to the dimensions of length scale multiplied by velocity scale. The velocity gradient is used as a velocity scale and physical length is used as length scale so we obtain

$$\nu_t = \frac{\mu_t}{\rho} = l_m^2 \frac{du}{dy} \qquad \text{(2-31)}$$

where ν_t is the turbulent kinematic viscosity; l_m is the mixing length (determined experimentally); y is the coordinate normal to the wall. These models are quite basic and

they work well only for flows that are characterized by a single length scale. In addition, l_m is unknown and must be determined [10].

2.2.2.2 One equation models

One equation models solve one turbulent transport equation for turbulent kinetic energy defined by Eq.   (2-7). In this model the velocity scale is proportional to the square root of the kinetic energy (different from the previous model where velocity is proportional to velocity gradient). Therefore, one can get [10].

$$\mu_t = C_m l_m \sqrt{k} \qquad (\text{2-32})$$

where C_m is a constant. A differential equation is developed for k :

$$\frac{\partial k}{\partial t} + U_i \frac{\partial k}{\partial x_i} = \frac{1}{\sigma} \frac{\partial}{\partial x_j} \left[(\nu + \nu_t) \frac{\partial k}{\partial x_i} \right] + P(k) - D(k) \qquad (\text{2-33})$$

Left hand side terms of Eq. (2-33) represent the convective transport of k. The first term on the right hand side is the diffusion term; the functions $P(k)$ and $D(k)$ on the right hand side represent the production and dissipation of k. $P(k)$ is function of the eddy viscosity and the fluid strain. One of the well-known one equation models is the Spalart-Allmaras model where transport equation is written for ν_t. Spalart-Allmaras model work well for aerospace engineering applications, such as flows over an airfoil. The poor performance of that model is seen in applications where length scale changes rapidly from wall region to free shear region. Therefore, it does not work for free jets, adverse pressure gradient flows and separated flows [10].

2.2.2.3 Two equation models

There are several two equation models which use the turbulent kinetic energy k and a second transport equation to have a closed system with well-defined turbulent scales. The most common forms of the second transport equation solve for the turbulent dissipation rate ε or turbulent specific dissipation rate ω . Some models are valid all the way to the wall (Low Reynolds Number models) and some models are valid outside the inner region of the boundary layer (high Reynolds Number models). The transport equation for k is derived from Navier Stokes equation with a form similar to Eq. (2-33). The square root of the turbulent kinetic energy can represent the velocity scale for large eddies. Therefore, we can use the definition of the turbulent length scale of the large eddies in equation (2-8) to obtain:

$$\nu_t = C_\mu \frac{k^2}{\varepsilon} \tag{2-34}$$

When deriving a transport equation for turbulent dissipation from Navier stokes equation, the equation contains fluctuating terms that cannot be modeled easily. Therefore, transport equations for ε and ω with production and dissipation terms are used. Turbulent specific dissipation rate ω is defined as

$$\omega = \frac{\varepsilon}{C_\mu k} \tag{2-35}$$

➢ **Standard $k - \varepsilon$ model**

The standard form of the ε transport equation is

$$\frac{\partial \varepsilon}{\partial t} + U_i \frac{\partial \varepsilon}{\partial x_i} = \frac{\partial}{\partial x_i}\left[\left(\nu + \frac{\nu_t}{\sigma_\varepsilon}\right)\frac{\partial \varepsilon}{\partial x_i}\right] + C_{\varepsilon 1}f_{\varepsilon 1}\frac{\varepsilon}{k}P_k + C_{\varepsilon 2}f_{\varepsilon 2}\frac{\varepsilon^2}{k} \tag{2-36}$$

Production and dissipation terms are formed from production and dissipation terms of turbulent kinetic energy equation scaled by $\frac{\varepsilon}{k}$ and multiplied by empirical constants and wall damping functions ($C_{\varepsilon 1} f_{\varepsilon 1}$, $C_{\varepsilon 2} f_{\varepsilon 2}$). Additional damping term is needed in the $k - \varepsilon$ model for applications near wall. Constants are determined by comparison with experimental data. Standard $k - \varepsilon$ model by Launder and Spalding [14] is the most widely validated turbulence model. It is somewhat more expensive than mixing length model. Its performance is poor in rotating flows and flows driven by anisotropy of Reynolds stresses. The weakness of the model lies with the modeled equations for ε. It needs tuning of the constants for different applications [10].

> **Improved $k - \varepsilon$ model (Launder and Sharma)**

It is a low Reynolds number $k - \varepsilon$ model which was derived by Launder and Sharma in 1974 [15**]**. The eddy viscosity relationship for the low Reynolds number model is

$$\nu_t = C_\mu f_\mu \frac{k^2}{\varepsilon} \qquad (2\text{-}37)$$

For the Launder and Sharma model, damping function f_μ is dependent on the turbulent Reynolds number, Re_t, as following

$$f_\mu = \exp\left(\frac{-3.4}{(1 + Re_t/50)^2}\right) \qquad (2\text{-}38)$$

$$Re_t = \frac{k^2}{\nu \varepsilon} y^+ \qquad (2\text{-}39)$$

where y^+ is the distance to the wall made non- dimensionalized with the friction velocity and kinematic viscosity:

$$y^+ = \frac{u_\tau y}{\nu} \qquad (2\text{-}40)$$

where u_τ is the friction velocity, y is the distance to the wall and ν is the kinematic viscosity of the fluid. At low Re_t values (near the wall) the damping function f_μ adjusts the turbulent viscosity. It increases the dissipation term, near the wall, to reduce the turbulence length scale otherwise the model will over-predict the turbulent viscosity. This damping function is not universal so it may need to be changed for different flow patterns [12].

> **Realizable $k - \varepsilon$ model**

It is a recent development of the traditional $k - \varepsilon$ model **[16]**. It contains a new formula for the turbulent viscosity and a new equation for ε. It is called realizable because it satisfies mathematical constraint on the Reynolds stresses consistent with the physics. To understand the meaning of realizable mode, equations (2-29) and (2-34) are considered to obtain an expression of the normal Reynolds stress:

$$\overline{u'^2} = \frac{2k}{3} - 2\nu_t \frac{\partial u}{\partial x} \tag{ 2-41}$$

In case of high strain fields, $\overline{u^2}$ may become negative (not physical). To make sure that $\overline{u'^2}$ is positive, from equations (2-41) and (2-34), we get the condition:

$$\frac{k}{\varepsilon} \frac{\partial u}{\partial x} > \frac{1}{3C_\mu} \tag{ 2-42}$$

To ensure the reliability (positivity) of normal stresses C_μ is made variable. The benefit of this model is that it predicts better the spreading of jets. It also provides better performance for flows involving rotation, separation and circulation [12].

> ➢ $k - \omega$ **model by Wilcox**

Wilcox [17] formulated a transport equation for ω

$$\frac{\partial \omega}{\partial t} + U_i \frac{\partial \omega}{\partial x_i} = \frac{\partial}{\partial x_i}\left[\left(\nu + \frac{\nu_t}{\sigma_\omega}\right)\frac{\partial \omega}{\partial x_i}\right] + \left[\beta - \frac{\kappa^2}{\sigma_\omega \sqrt{C_\mu}}\right]\frac{\omega}{k}P_k - \beta \omega^2 \qquad (2\text{-}43)$$

This equation is similar to ε transport equation. It is derived for wall bounded flows so it requires no additional damping term in boundary layer flows. Compared to $k - \varepsilon$ model, $k - \omega$ model has shown to be more sensitive to the free stream value of ω and performs better at walls. It does not need much tuning of the constants similar to $k - \omega$ Model [10].

> ➢ **Shear Stress Transport (SST) model by Menter**

In general, $k - \varepsilon$ models are more accurate in shear type flows while $k - \omega$ models work well in the near wall region. Therefore, Menter [18] developed a model which behaves like $k - \omega$ close to the wall and switches to $k - \varepsilon$ model away from the wall. To achieve this, $k - \varepsilon$ model is converted into $k - \omega$ formulation. Both models are multiplied by blending function. Blending function is designed to be one in the near wall region to activate Wilcox model and zero away from the surface to activate $k - \varepsilon$ model. It is called Shear Stress Transport model because it used the shear stress relationship that the shear stress is proportional to the turbulent kinetic energy:

$$-\overline{u'v'} = a_1 k \qquad (2\text{-}44)$$

where a_1 is a constant.

SST model proved to be one of the most accurate two-equation models for flow separation prediction. It is also more accurate for shock waves and adverse pressure gradient flows [10]. We have summarized turbulence models in Table 2.2.

Table 2.2: Different applications for different turbulence models

Turbulence model	Applications
$k - \varepsilon$ model (Launder and Spalding, 1972)	More accurate in free shear flows. Poor in rotating flows. It needs tuning of parameters.
$k - \varepsilon$ model (Launder and Sharma, 1974)	Low Reynolds number model (decreases the turbulent viscosity near the walls).
Realizable $k - \varepsilon$ model (Shih, 1995)	Better for jet spreading, recirculation.
$k - \omega$ model (Wilcox, 1988)	It is derived for wall bounded flows. Does not need much tuning of constants. More sensitive to inlet boundary conditions.
Shear Stress Transport $k - \omega$ model (Menter, 1993)	$k - \omega$ near the wall and $k - \varepsilon$ in free shear flows. Better for separation flow and adverse pressure gradient flows.

3   Steam blowdown results

This chapter starts by a description of the simulation setup and the initial results in section 3.1. In section 3.2 we attempt to assess our results and show the uncertainty relevant to turbulence modeling. Finally, results from OpenFOAM simulation using SST $k - \omega$ turbulence model are presented. The reasons behind selecting this model are explained in section 4.2.

Table 3.1: System parameters used in simulation case study.

Fluid volume	
Reactor pressure vessel (RPV)	950 m^3
Lower drywell (LDW)	1190 m^3
Upper drywell (UDW)	6016 m^3
Initial (pre-DCH) system conditions	
Pressure in RPV/RCS	8.5 MPa
Temperature in RPV/RCS	800 K
Containment pressure	0.25 MPa
Containment temperature	401 K
Vessel hole diameter	1 m

3.1 Description of the actual work

A 3D computational mesh was designed according to the data in [3] tabulated in Table 3.1. Figure 3.1 and Figure 3.2 depict a simplified design of an ESBWR containment and mesh designed by OpenFOAM. Since the reactor internals and many containment structures and components are not modeled, dimensions are adjusted to conserve the fluid volume. For example, the reactor pressure vessel (RPV) height is reduced to reflect the volume of reactor coolant system (RCS). While the drywell height is prototypal, the lower drywell (LDW) and upper drywell (UDW) diameter is adjusted to reflect the volume available for fluid. Suppression pool effect is not considered and the presence of the control rods and corium is not included in this initial study.

A major set of simulations was then performed with a mesh of 1.14 million nodes. The system's total mass and total energy are checked and found to be conserved with high accuracy (0.081% and 0.56%, respectively, see Figure 3.3 and Figure 3.4. Total energy is calculated as the sum of thermal energy and kinetic energy. The simulations were performed with and without turbulence models. In the latter case, the simulations effectively use the under-resolved grid numerical diffusion as an implicit sub-grid scale turbulence model. However, the grid resolution (in case with ~1 million nodes, $\Delta x = \Delta y = 0.14m, \Delta z = 0.0364m$) is not fine enough for capturing large eddies. The transient temperature and pressure field in the RPV, LDW and UDW are mass-averaged to obtain parameters that are compared to lumped - parameter predictions by a transient CLCH model. Appendix B illustrates some simulation snapshots for blowdown progression.
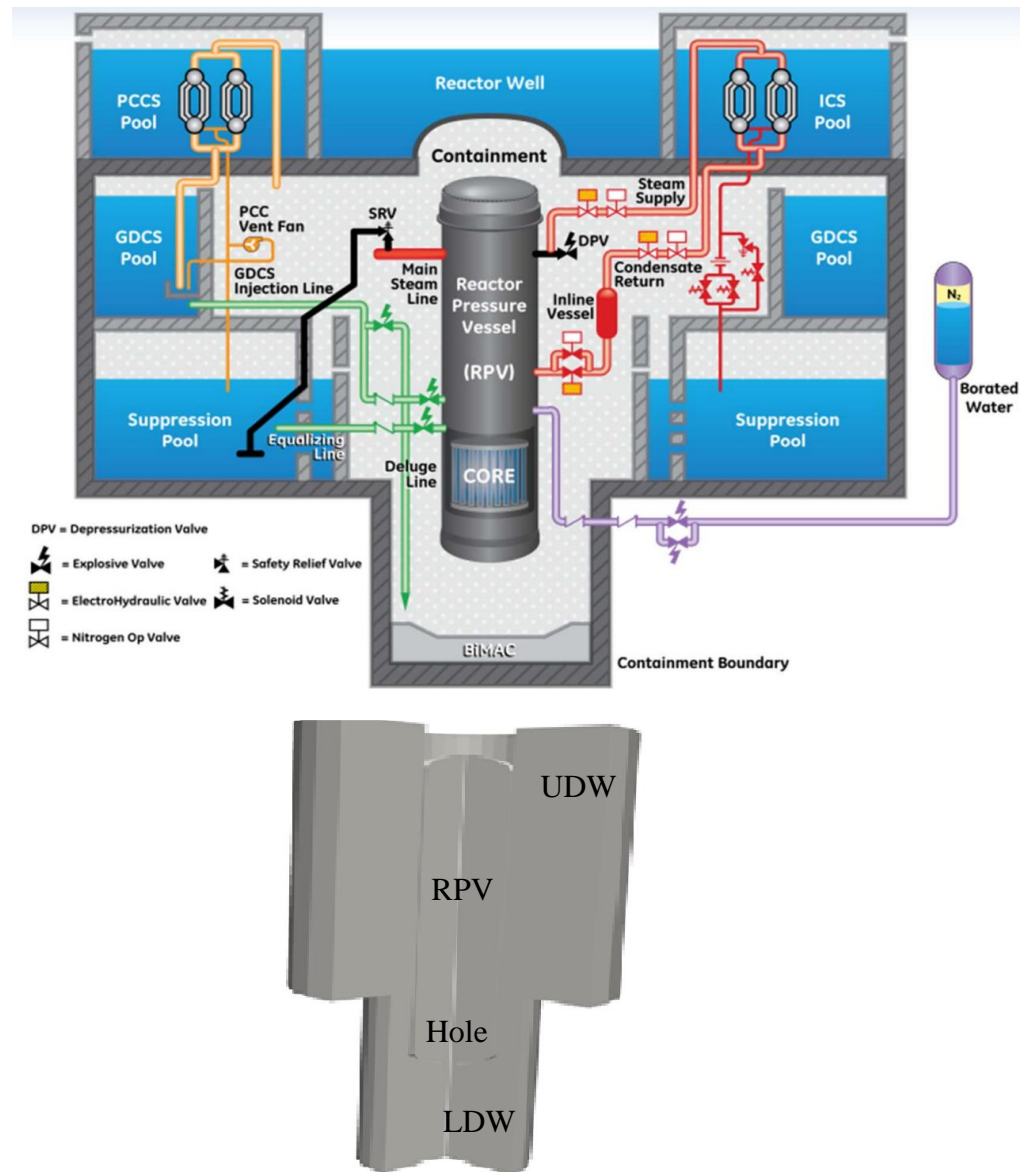
Figure 3.1: Computational domain (below) representing actual ESBWR containment design (above).
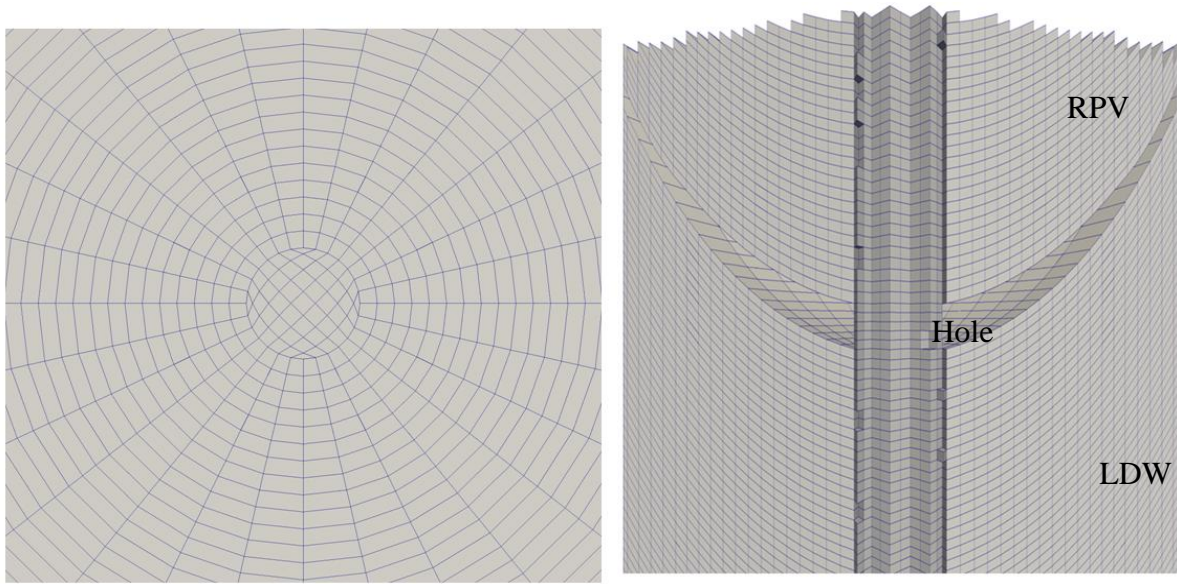
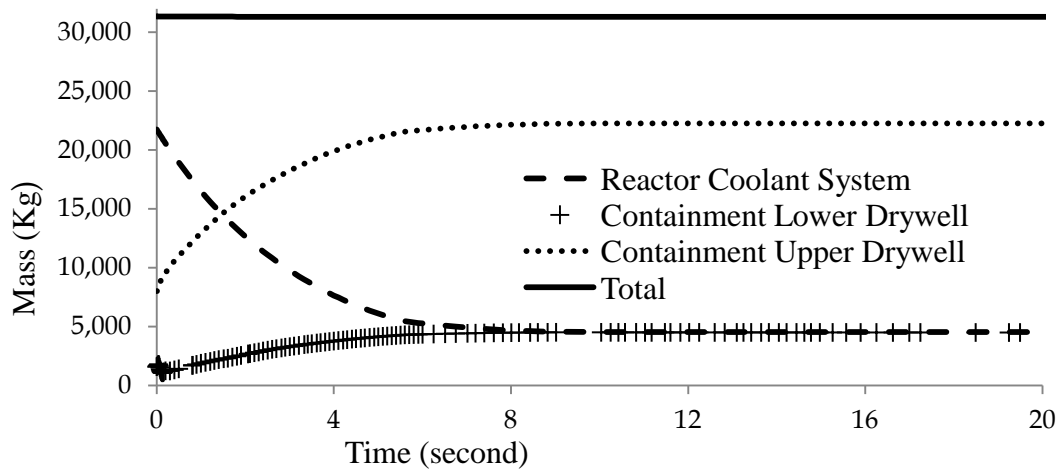**Figure 3.2: Mesh configuration: horizontal view (left) and plan view (right).**

Figure 3.3: Change of mass during steam blowdown from reactor coolant system to containment.
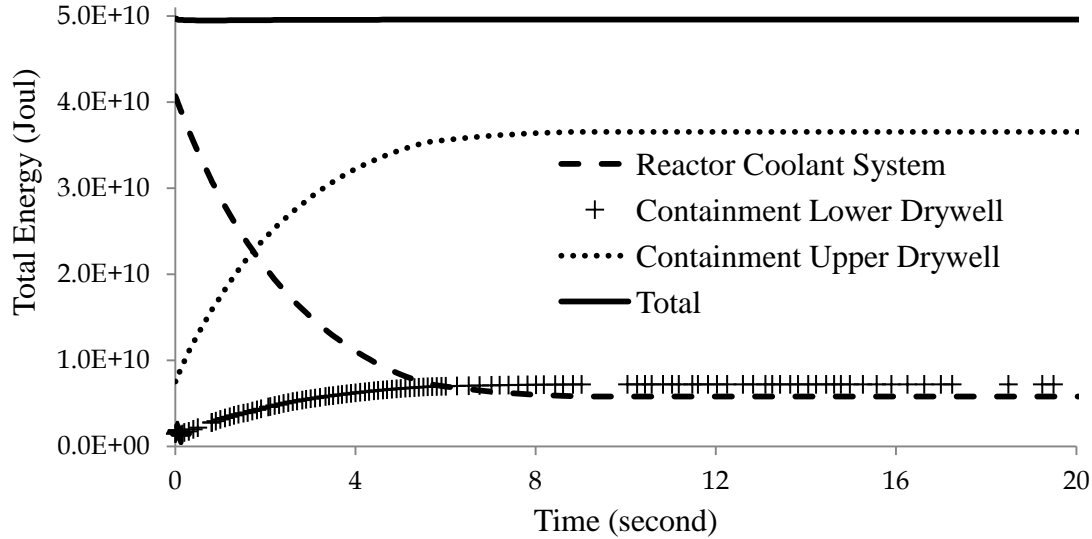
Figure 3.4: Change of total energy during steam blowdown from reactor coolant system to containment.

3.2 Model assessment

Blowdown situation involves several characteristic flow patterns such as jet flow, jet impingement, wall spreading flow and recirculation phenomena (discussed in detail in section 4.1.4 and Figure 4.6). These phenomena, individually or in combination, have been investigated in the past. Direct comparison of previous work is hindered by differences in geometry, jet to target distance, pressure ratio, Mach number, Reynolds number. This complex flow pattern requires a systematic evaluation of the CFD capability (see chapter 4). The effect of turbulence modeling on the predicted local behavior is demonstrated in Figure 3.5. Figure 3.5 compares the jet structure with data from simulation described in a previous computational work [19], where a high constant pressure boundary condition was imposed at the inlet of the nozzle and the cylinder pressure was held constant. The simulations were

performed using three different treatments of turbulence: no turbulence model, realizable $k - \varepsilon$ and SST $k - \omega$ turbulence models.

In Figure 3.5, x/d is the distance, along the jet centerline starting from the nozzle outlet center to the bottom of the containment, normalized by the nozzle diameter; P/P_n is the pressure along the jet centerline normalized by the nozzle outlet center. OpenFOAM results show a good agreement with the previous results experimental results in Figure 3.5. The jet pressure distribution is the same for different pressure ratios at a given distance. For OpenFOAM simulation, because pressure ratio is not constant as there is no inlet or outlet boundary conditions, pressure ratios are calculated for any given time moment. Figure 3.6 shows that compartment-averaged pressure and temperature, particularly in the LDW, are sensitive to treatment of turbulence. For the LDW, peak temperature variation is 48.6 K.
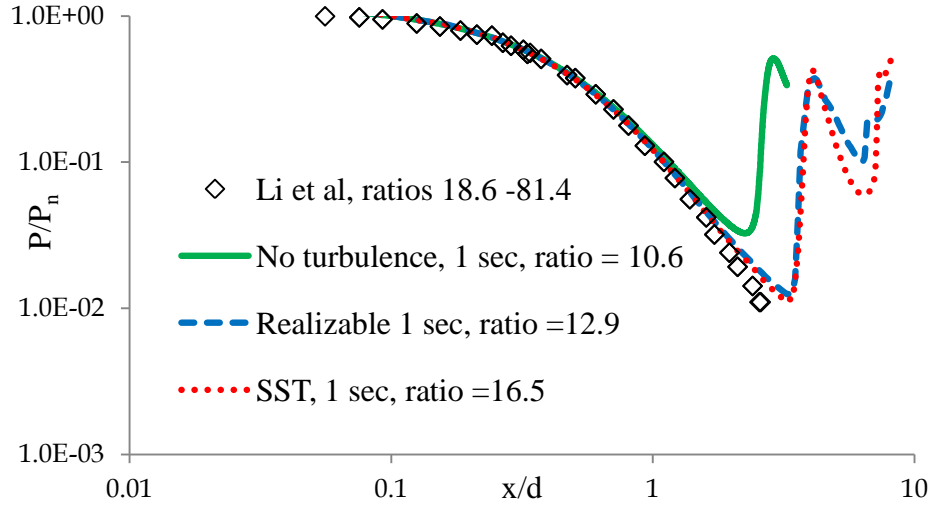
Figure 3.5: Effect of overall pressure ratio on the local non-dimensional pressure profile along jet centerline.
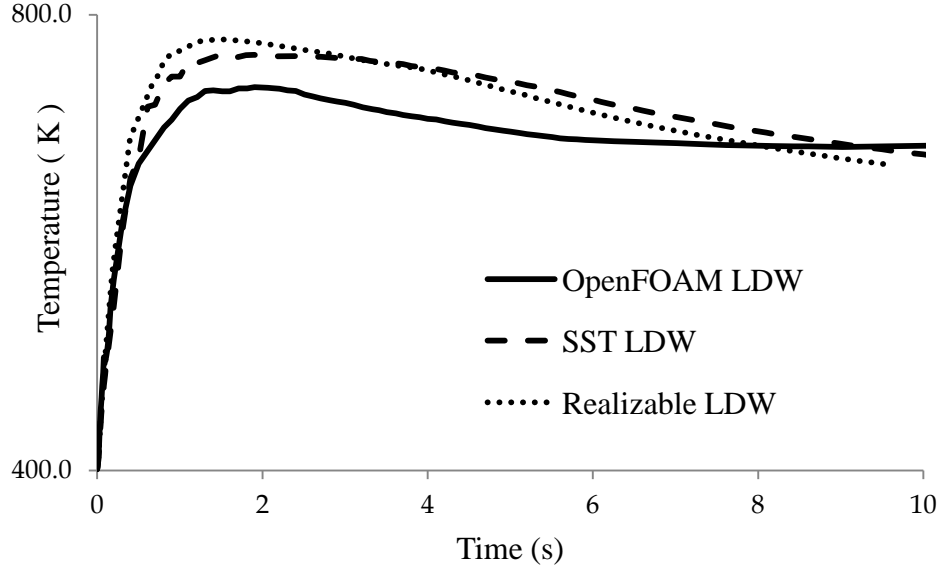
Figure 3.6: LDW temperature sensitivity to turbulence models: realizable (k-ε) and SST.

3.3 Simulation results

Figure 3.7 and Figure 3.8 depict OpenFOAM results and predictions by the transient version of the lumped-parameter CLCH model [3] with modification per Chang [20]. While the trends are similar between the 3D CFD simulation and the CLCH model, there remain significant differences in LDW temperature. This difference may be attributed to different discharge coefficient that causes a difference in cooling rate in the LDW. Analysis of transient fields reveals a large variation of local pressure and temperature in the LDW and UDW (Figure 3.9 and Figure 3.10). A broad range of temperature and pressure in LDW demonstrates that this variation cannot be captured by the lumped-parameter model. Given the interactions that occur locally, and depend on local pressure and temperature, the compartment-averaged quantities are unable to accurately capture the phenomena occurring at the edge of the parameter ranges.
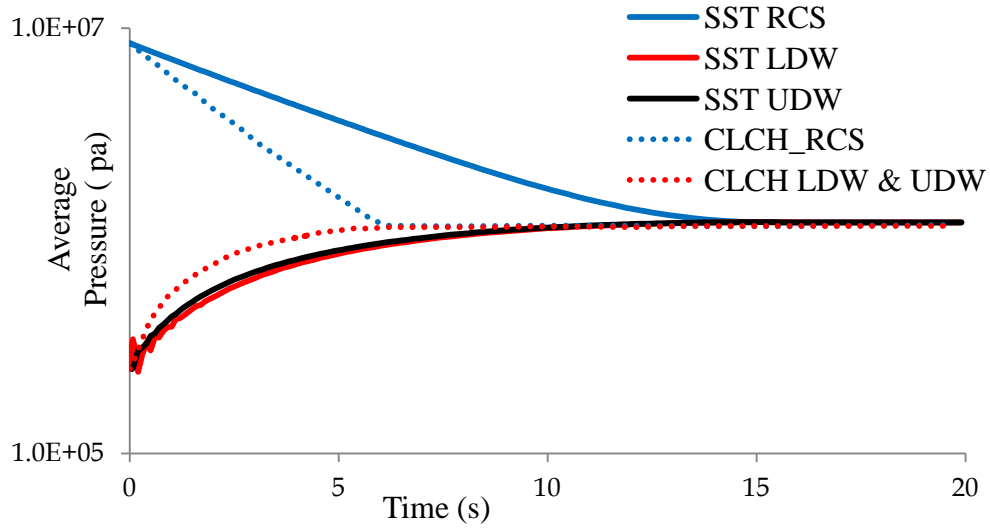
Figure 3.7: Comparison between OpenFOAM (SST model) results and CLCH model results. The simulation indicates an over estimate of discharge coefficient (0.85) used in the lumped-parameter CLCH model.
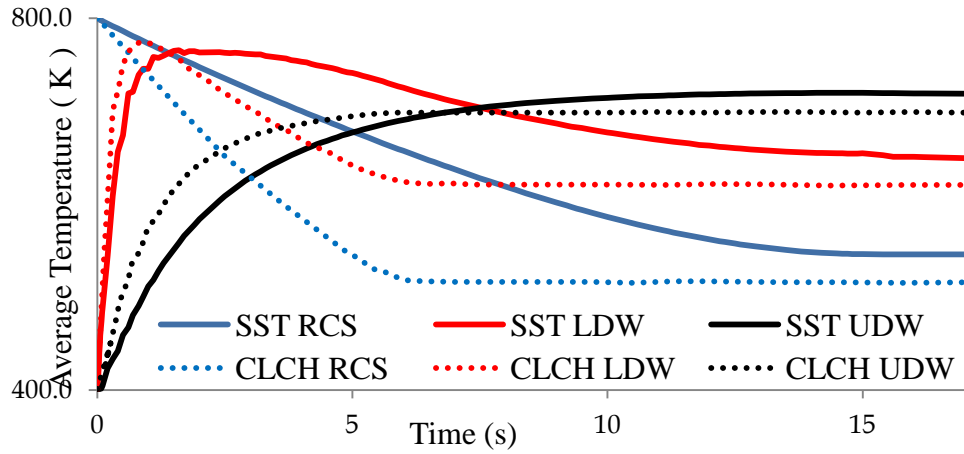
Figure 3.8: Comparison between the OpenFOAM (SST model) results and the CLCH model results. More rapid cool down in RCS predicted by CLCH is attributed to the high discharge coefficient.
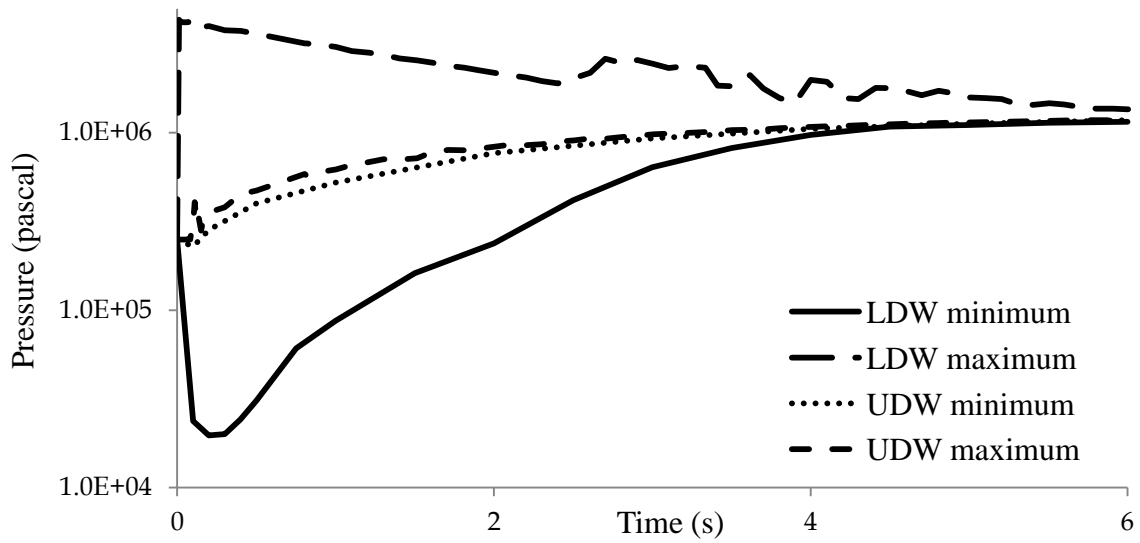
Figure 3.9: Calculated maximum and minimum pressures for the LDW and UDW depict a wide pressure variation in the LDW.
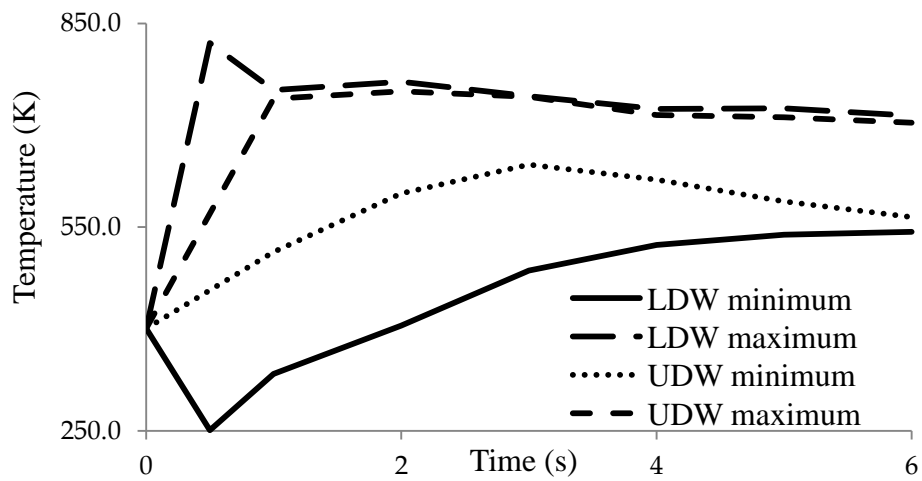
Figure 3.10: Calculated maximum and minimum temperatures for the LDW and UDW depict a wide temperature variation in the LDW

4 Evaluation model development and assessment process

EMDAP is a systematic process described by NRC to assess the models used in nuclear accident calculations and to estimate and reduce uncertainty of these models. Evaluation Model (EM) is the whole framework of calculations. In our case EM includes: (i) OpenFOAM CFD solver; (ii) turbulence models; (iii) computational meshes; (iv) thermodynamic and transport properties. The following additional components are also part of EM: (v) initial assumptions; (vi) postulated scenario; (vii) initial and boundary conditions. EMDAP process consists of the following elements [21]:

1. Establish Requirements for Evaluation Model Capability.
2. Develop Assessment Base.
3. Develop Evaluation Model.
4. Assess Evaluation Model Adequacy.

The relation between the 4 Elements is illustrated in Figure 4.1. Steps, within each element, are described and applied to the problem under consideration in the following sections.

4.1 Requirements for evaluation model capability

The first element of EMDAP process is identifying the major application of the evaluation model. In subsection 4.1.1, the analysis purpose and the power plant class are identified. Choosing the figure of merit is explained in subsection 4.1.2. This leads to specify the systems, components, geometries and phases which need to be modeled (subsection 4.1.3). For each component or geometry, different phenomena are identified, ranked and detailed in subsection 4.1.4.

Establish requirements for evaluation model capability

(1) Specify analysis purpose, transient class and power plant class.

(2) Specify figures of merit.

(3) Identify systems, components, phases, geometries, fields that should be modeled.

(4)Identify and rank phenomena and processes.

Develop assessment base

(5)Objectives for assessment base.

(6) Scaling analysis.

(7) Integral effect testing and separate effect testing to complete the database.

(8) Evaluating effects of Integral effects distortion and separate effect scale up.

(9)Determine experimental uncertainty.

Develop evaluation model

(10) Establish EM development plan.

(11) EM structure.

(12) Develop Closure Models.

Assess evaluation model adequacy
Does Code meets adequacy standard ?

Figure 4.1: Elements of Evaluation Model Development and Assessment [21].

4.1.1 Analysis purpose

In this work, steam blowdown, which is a phenomenon in DCH, is studied using CFD software package, OpenFOAM [4]. OpenFOAM is applied to simulate transient, multi-dimensional single-phase flow in Economic Simplified Boiling Water Reactor (ESBWR) containment in a beyond design basis accident (B-DBA). We choose to perform this

simulation for ESBWR configuration, for which information and data about the containment system geometry, scenarios, and predictions are available [3, 22].

This study is done as a prerequisite for simulating the whole DCH scenario which is dominated by the corium energy. Corium is expected to relocate to the LDW so focus here would be on LDW phenomena which include: (i) steam blowdown, (ii) steam jet impingement and (iii) convective mixing. The suppression pool effect is not considered and the presence of the control rods and corium is not included in this initial study. A circular hole at the bottom of the pressure vessel is assumed to instantly form in the beginning of the simulation. In other words, the process of the hole ablation is ignored. Probabilities of events leading to the assumed scenarios are not considered now because the project's goal is to assess CFD's capability to handle such extreme scenarios.

4.1.2   Figure of merit

In a DCH scenario, spreading and entertainment of corium depend on the momentum of the blowdown steam impinging upon the corium layer. Since this study focuses on validation of CFD capability to describe the blowdown process, the Figure of Merit in this case are flow characteristics that are measured in validation experiments.   Such characteristics include: (i) pressure profile along the jet centerline; (ii) Mach number along the jet centerline and (iii) Mach disk location.

4.1.3   Systems and components that should be modeled

The purpose of this step is to identify the evaluation model characteristics. Different items that are needed to be modeled are shown in Figure 4.2. Simplifying the simulation by designing 3D 30-degree wedge and half geometry domains did not produce the same results

of full geometry design and this is mostly attributed to the difficulty of simulating non symmetrical three-dimensional flows without the full geometry design (Figure 4.3 and Figure 4.4). Introduction of the additional (symmetric) constraints in highly dynamic, inherently unstable blowdown jets results in the non-physical jet behavior (Figure 4.5).

4.1.4 Phenomena identification and ranking

Development of the Phenomena Identification and Ranking Table (PIRT) aims to identify and prioritize important physical phenomena in the system/ process of interest. PIRT's function is to ensure that we focus on the activities that will impact the figure of merit. Prioritization is derived from an importance ranking of the phenomena relative to the main requirements. Melt energy transported by steam is the main concern which is the basis for assessing the importance of simulation accuracy of any single phenomenon. PIRT also includes columns for assessing code adequacy and validation adequacy. PIRT is used to be more specific about the fidelity of our simulation. Each phenomenon has its characteristic parameters. In the following subsections we identify different phenomena and for each phenomenon, its characteristic parameters are related to the figure of merit [21]. Most of the interesting phenomena are demonstrated in Figure 4.6 by the numbers, which label the location of each phenomenon. To narrow down the focus of the problem, the importance of the Upper Drywell (UDW) is ranked to be low because steam role in entraining and dispersing the melt is located in the Lower Drywell (LDW).

4.1.4.1 Flow discharge

When the high pressure steam in the reactor pressure vessel (RPV) passes through the hole into the low pressure containment, steam velocity increases because it flows through a small cross section area. Initially, the RPV pressure is much higher than the containment

pressure so the flow velocity at the hole exit is at a sonic condition, i.e. Mach number equals one and this results in the flow choking. The pressure ratio below which flow is not choked is called the critical pressure ratio.

To identify the importance of both choked and non-choked flow, we identify the half life, $t_{1/2}$, as the time needed to reduce RCS pressure by 50%. Period of interest, when most of melt dispersal process occurs, is assumed to be $2t_{1/2}$. Initial results as shown in Figure 4.7 and Figure 4.8, reflect the uncertainty in the solver (pressure based solver and density based solver) and also in the turbulence modeling approach. In Figure 4.7, $2t_{1/2} = 4$ Sec or 8 Sec for laminar and turbulent flows, respectively. In Figure 4.8, $2t_{1/2}$ of the 4 cases is always corresponding to pressure ratios around 2. Therefore, non-choked flow region is given a low importance ranking.

System

- ESBWR free volume (volume available for steam)

Components

- Pressure vessel, PV Hole, Containment compartments: LDW and UDW

Phase

- Steam (gas) for blowdown and mixing processes. Containment air isn't as important as steam for this initial study.

Geometry

- Three dimensional full geometry is needed. The CFD 3D simulations were also performed for a 1/12 segment (30-degree wedge) and a ½ segment of an axisymmetric containment. The results obtained exhibit notable differences from results of full geometry simulation. This outcome is attributed to the difficulty of introducing additional (symmetrization) constraints in highly dynamic, inherently unstable blowdown jets.

Fields and Transport Processes

- Mass and energy are transported from PV to containment so mass and energy conservation are required. Processes included are blowdown, jet flow and impingement, wall spreading flow and recirculation.

Figure 4.2: Systems, components, phases, geometries, fields and processes that should be modeled.
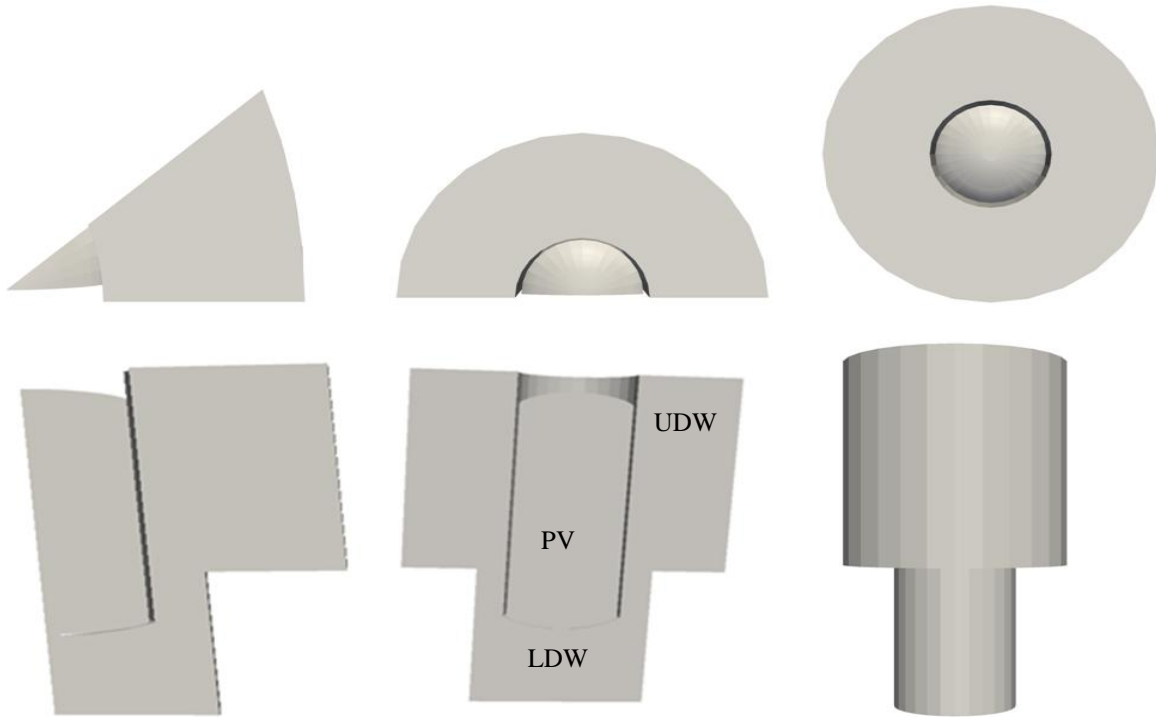
Figure 4.3: Different designs (from left to right): 30-degree wedge, half geometry and full scale geometry. The upper row is the top view and the lower row is the side view. Components are demonstrated on the half geometry side view. PV: Pressure Vessel. LDW and UDW are Containment compartments: Lower Dry Well and Upper Dry Well.

At the nozzle (hole) end, the actual mass flow rate is different from the theoretical flow rate which assumes in-viscid one-dimensional ideal gas flow. The ratio of the actual discharge to the theoretical discharge is the discharge coefficient. Discharge coefficient is dependent on the nozzle shape and Reynolds number which is highly variable in our case. Therefore, we expect that discharge coefficient may be time-dependent. Accuracy of the turbulence modeling is essential to compute the correct discharge coefficient.
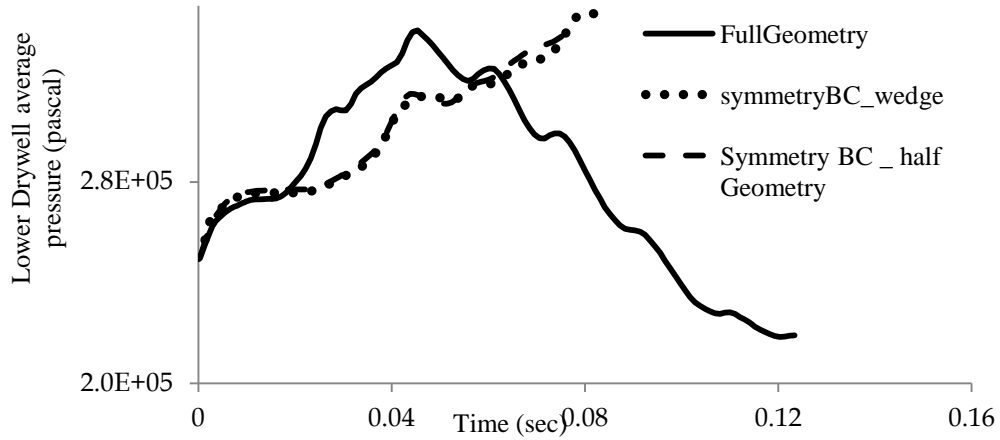
Figure 4.4: Comparison between wedge, half geometry and full geometry.

4.1.4.2 Under-expanded sonic jet flow

The first flow region is the jet flow. Under-expanded jet emerges from the hole in the RPV and the expansion waves reflect at the jet boundary as compression waves. For the choked flow, the compression waves meet and form Mach disks. For lower pressure ratios, boundary reflection process does not include shocks. In both cases, jet shows a periodic behavior of the state parameters along the symmetry axis for a certain downstream distance, then the damped periodic behavior is overcome by turbulence and molecular diffusion [19, 23]. The global behavior of the steam can be related to jet axial parameters like Mach disk location, axial Mach number, axial pressure profile and axial velocity profile. These parameters depend on axial distance and pressure ratio.

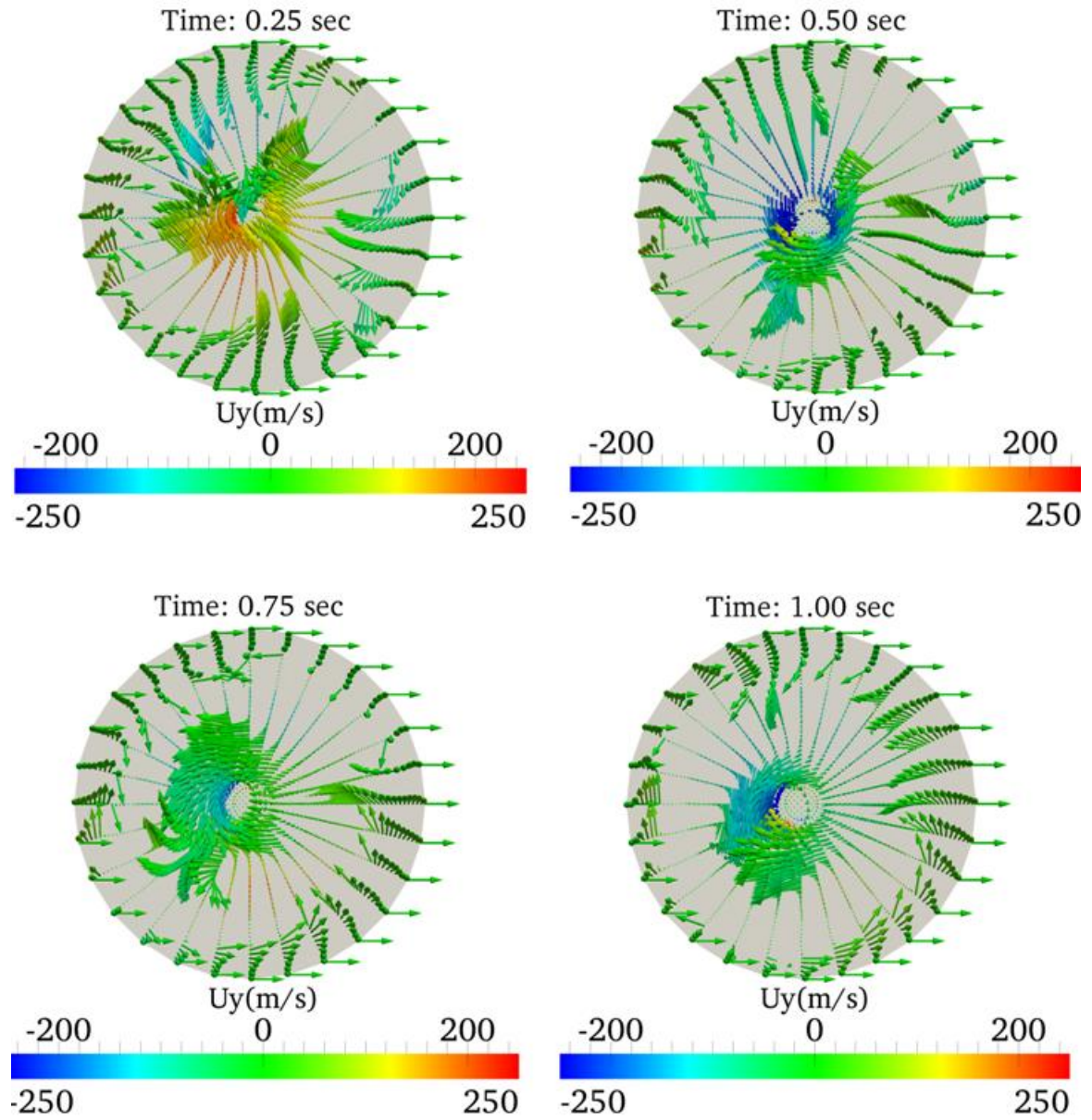**Figure 4.5: Velocity field (y-direction) at the nozzle outlet (unstable circular motions).**

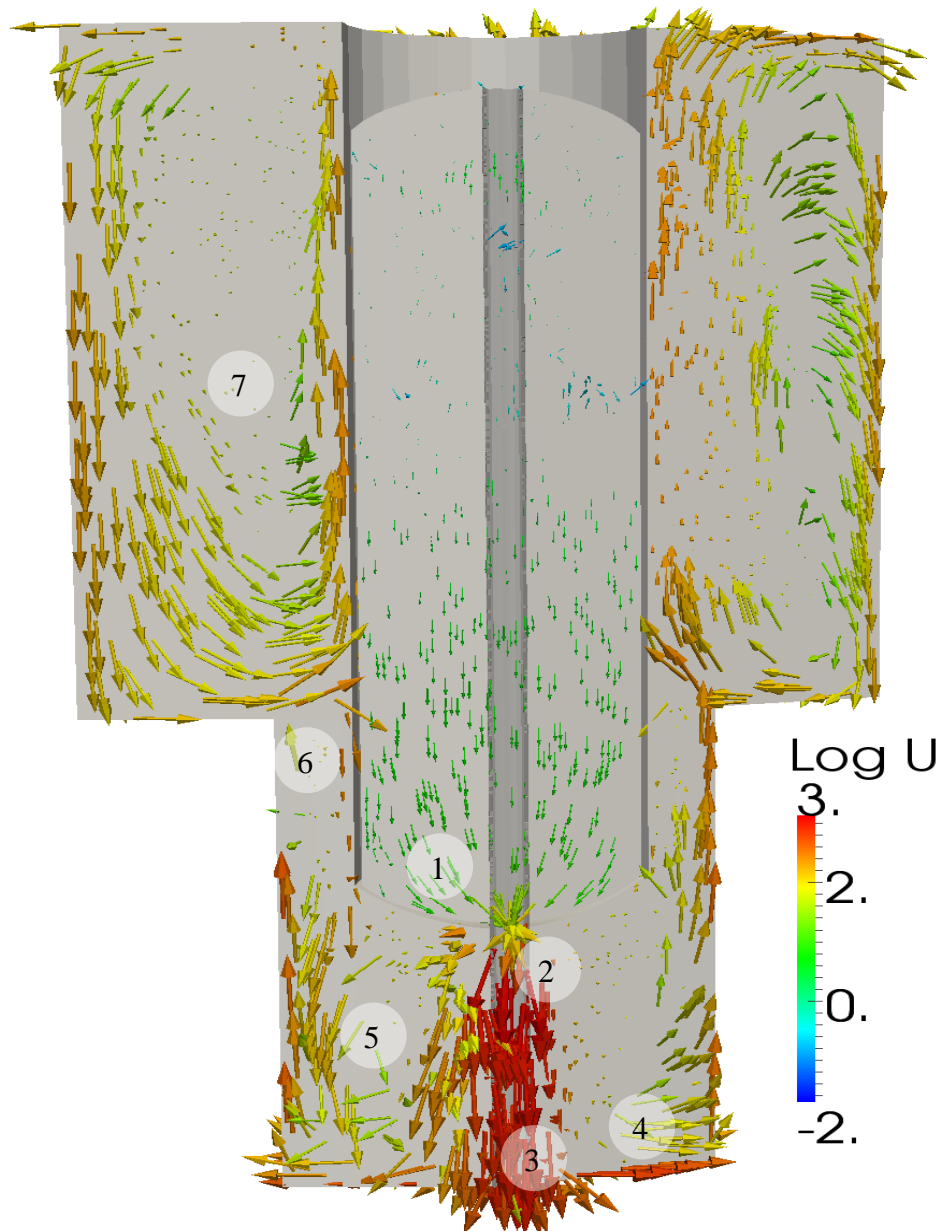**Figure 4.6: Computation domain representing ESBWR containment design. Steam velocity is shown (Log scale) at t=1sec after blowdown initiation. Phenomena included are: 1-Flow discharge, 2- Jet flow and instability, 3-Jet impingement, 4-Wall Jet, 5- Recirculation flow, 6-Orifice Flow, 7- Mixed Convection.**

Figure 4.7: Transient behavior of RCS pressure normalized to its initial value. Results for pressure based and density based solvers with laminar model and turbulence models (SST and Realizable $k - \varepsilon$ turbulence model).
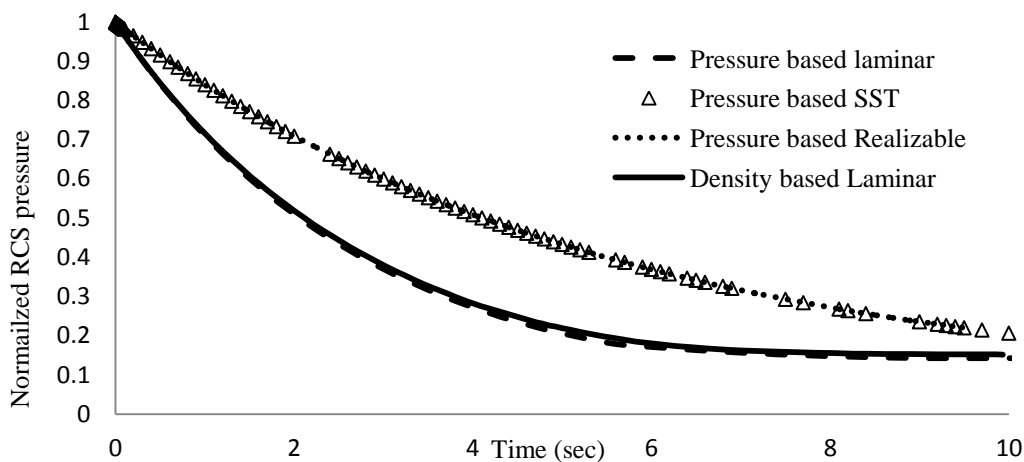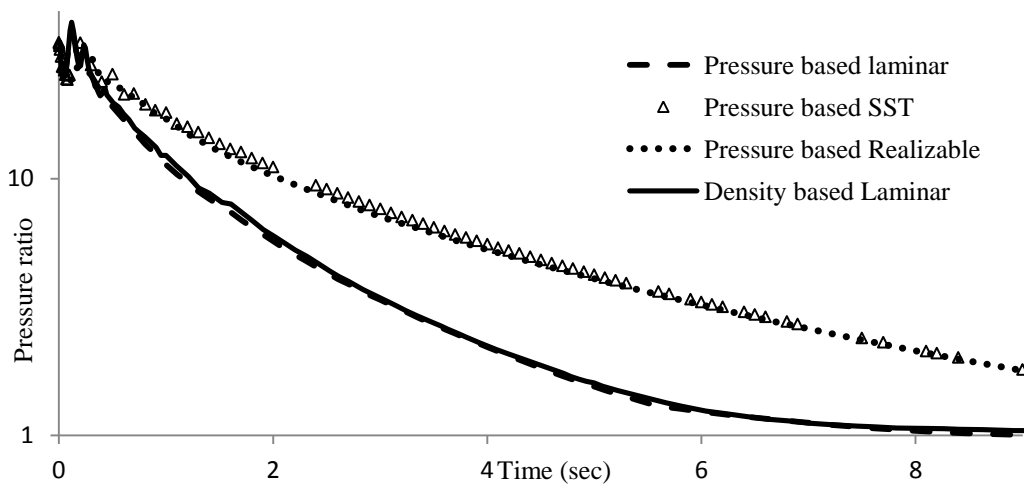

Figure 4.8: Transient behavior of Pressure ratio. Results for pressure based and density based solvers with laminar and turbulence models. (SST: shear stress transport model and Realizable: Realizable $k - \varepsilon$ turbulence model). Pressure ratio is the ratio between RCS pressure to LDW pressure.

4.1.4.3 Jet impingement

When the high-speed steam flow approaches the wall, its axial velocity goes to zero. As the jet slows down, kinetic energy is converted to thermal energy. The ratio between the thermal energy to kinetic energy is called the recovery factor. For highly turbulent jets $(R_e = 61,000 - 124,000)$ recovery factor depends mainly on the jet - wall spacing, H normalized by nozzle diameter, d, not on the Reynolds number [24]. Actual and theoretical recovery factors are the same for high values of H/d (>6). Flow and temperature fields are correlated with each other. Vortices are emanating from the jet nozzle and dominating the jet close the wall. Therefore, the jet separates due to interaction between primary vortices and the wall. Jet impingement is controlled mainly by Reynolds number and jet-wall spacing [25, 12].

4.1.4.4 Jet instability

The main source of turbulence is the velocity gradient which is present in the shear layer of the jet boundaries. The area of the shear layer increases along the jet axis. For high Reynolds number flow, the shear force effect becomes dominant. As the shear layer moves, oscillations develop and move from side to side. Downstream, oscillations grow to produce large eddies whose length scale is comparable to the jet diameter. Finally, eddies break into smaller eddies. The pressure field of the stagnation region displaces eddies laterally till they arrive at the wall. The development of turbulence affects the fluctuation of the velocity in radial direction [12].

4.1.4.5 Wall jet

Around the wall impingement location the jet flow decelerates, turns and becomes the wall jet. The wall jet moves horizontally parallel to the wall in radial direction. As it progresses, its speed decreases as it moves away from the wall. Because the jet impingement zone is unsteady, the wall jet is also unsteady. The shear layer vortices propagate into the wall jet. Moving away from the nozzle, the jet thickness increases. This thickness is evaluated by measuring the height at which the wall parallel velocity drops to 50% of the maximum radial speed of the wall jet. Wall jet properties are reported as a function of pressure ratio and nozzle/plate distance, *H/d* [26].

4.1.4.6 Recirculation flow

Interaction between the wall jet and the confinement surface creates a recirculation zone (big vortex). This zone is not noticed when studying free jets. The effect of Reynolds number on this zone is negligible. When the aspect ratio (cylinder height to its diameter) increases, the vortex length increases and its location moves downstream. Lower aspect ratio means that the wall jet is affected by the confinement surface close to the jet centerline so smaller vortex is produced [27].

4.1.4.7 Fluid properties

As steam is ejected from the nozzle, jet centerline axial pressure decreases to pressures less than the containment pressure. This decrease is corresponding to an increase in jet velocity and Mach number. Also, increase in jet velocity (kinetic energy) is accompanied by a decrease in internal energy so the jet centerline axial temperature decreases. Pressure

decrease and temperature decrease were reported before [19, 28]. For steam, this decrease in pressure and temperature to values lower than the initial pressure and temperature results in condensation and appearance of the liquid phase. This may reduce the high speed and high momentum of the jet.

4.1.4.8 Geometry impact

To ESBWR, pressure vessel bottom is penetrated by control rods and control rod drive. Therefore, steam blowdown consequences are probably overestimated because control rods are expected to hinder the jet flow. On the other hand, high temperature melt relocation at the lower plenum and ejection to the containment threatens the attachments of control rods. Therefore the assumption of control rod absence is quite feasible.

4.1.4.9 Orifice flow

The path between Lower Drywell and Upper Drywell is constricted by 8 large blocks which support the pressure vessel. Thus, 70% of the flow path between LDW and UDW is occupied [3]. This sudden reduction in cross sectional area would increase steam velocity and reduce its static pressure. Steam momentum at UDW and melt energy transport to UDW will be impacted by that constriction.

4.1.4.10 Mixed convection

In the problem under consideration, the mixed convection can be described as follows. Hot high pressure blowdown steam passes from Lower Drywell to Upper Drywell. Hot less dense steam moves to the top of UDW while hotter steam is coming from LDW so

steam stratification is unstable and thus results in mixing. Therefore heat is transferred, at UDW, by both pressure forces and buoyant forces. Natural convection spread the melt energy at the containment, however; this research focuses on melt entrainment and dispersion by highly energetic steam so low ranking is given to UDW natural convection.

4.1.4.11 Steam condensation

Fluid at Upper Drywell is initially less hot than hot steam at lower drywell. Therefore a fraction of steam may condense at UDW. The steam condensation rate is probably slow relative to the highly dynamic steam blowdown. Therefore condensation won't impact direct containment heating accident. Finally, all these phenomena are tabulated and ranked in Table 4.1.

4.2   Development of the assessment base

The second element of the EMDAP process is developing an assessment base using the requirements established before. The computational model needs to be validated against experimental data which address the phenomena. This includes performing experiments that are relevant to the considered scenario and assuring applicability of the models, based on these experiments, to full scale analysis of the plant [21]. In this thesis, CFD capability is assessed by validating its solvers against the results of two experiments. Based on the Phenomena Identification and Ranking Table, major physical phenomena are highly ranked. Two specific experiments, as shown in subsections 4.2.1 and 4.2.2, are selected to capture some of these important phenomena.

Table 4.1: Phenomena Identification and Ranking Table.

Module	Phenomena and effects		Rank
PV	Flow discharge	Choked flow	H
		Non-choked flow	L
LDW	Jet flow		H
	Jet impingement		H
	Jet instability		H
	Wall jet		H
	Recirculation		H
	Fluid properties		H
	Geometry impact		L
UDW	Orifice flow		L
	Mixed convection		L
	Steam condensation		L

Since the steam blowdown process occurs with high pressure gradient where the compressibility effects are important, the validation is done using OpenFOAM compressible solvers. Three different solvers are tested [4]:

1. *sonicFoam*: This is a transient pressure-based solver for trans-sonic/supersonic gas flow. It is considered because of the high ranking given to the sonic jet flow as explained previously.
2. *rhoCentralFoam*: This is a density-based compressible flow solver.
3. *compressibleMultiphaseInterFoam*: This solver is designed for two or more compressible fluids using volume of fluid phase fraction-based interface capturing approach. It is suitable for simulating the whole DCH phenomena.

4.2.1 Jet impingement and wall jet problem

First validation experiment is the jet impingement followed by wall jet as described in [29]. Subsection (A) gives a description of the problem and the problem setup. CFD capability is then evaluated by comparing numerical results to experimental data using different turbulence models and different OpenFOAM solvers in subsection (B). Conclusions and insights gained from the results are summarized in subsection (C).

A. Description

Figure 4.9 shows the turbulent jet discharged from a circular nozzle and then impinging on the bottom wall. The jet nozzle diameter, d, is 0.01m. The jet Reynolds number is 23,000 (based on the jet velocity, diameter and fluid viscosity). The distance from the jet nozzle to the impingement plate, H, is 6 nozzle diameters, ($H/d = 6$). Jet centerline to outlet distance is $20d$ (far from the jet to avoid the effect of the outlet boundary condition on the results). The simulation is done initially with non-uniform three dimensional meshes which are refined in the radial direction around the jet, Figure 4.10. The adopted grid size for initial computations is 104 (radial) $\times$ 90 (normal to the plate). Experimental data are given in terms of the bulk velocity of the nozzle so the inlet section is designed to be outside the main domain at the distance of half the nozzle diameter. This added nozzle helps to introduce more realistic turbulent velocity profile at the nozzle exit, Figure 4.11.

The boundary conditions are as follows:

Pressure: Zero gradient at all the boundaries.

Temperature: Zero gradient at all boundaries (adiabatic).

Velocity: Inlet velocity is 35.6 m/s, equivalent to the jet Reynolds number, 23,000. No slip (zero velocity) boundary condition is imposed at the walls. Boundary condition at the outlet: zero gradient. The width of the domain is large enough so the simulation results obtained at the central part of the domain are not sensitive to the outlet boundary condition.

Turbulence parameters (k, ε, ω): Turbulent inflow conditions were calculated based on inlet velocity and low turbulence intensity, 0.05. Turbulence intensity is defined as

$$I = \frac{u'}{U} \tag{4-1}$$

where u' is the root-mean-square of the turbulent velocity fluctuations and U is the mean velocity.
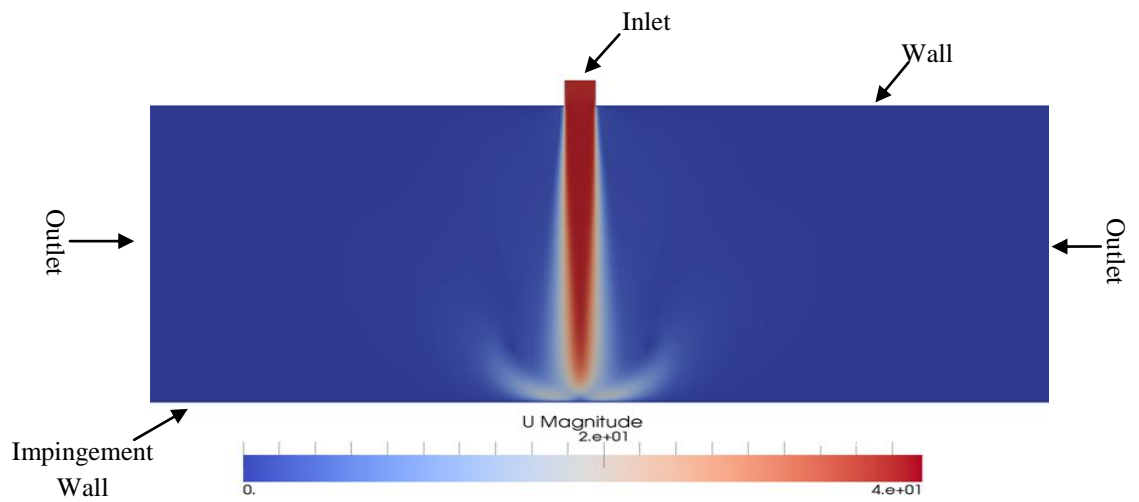
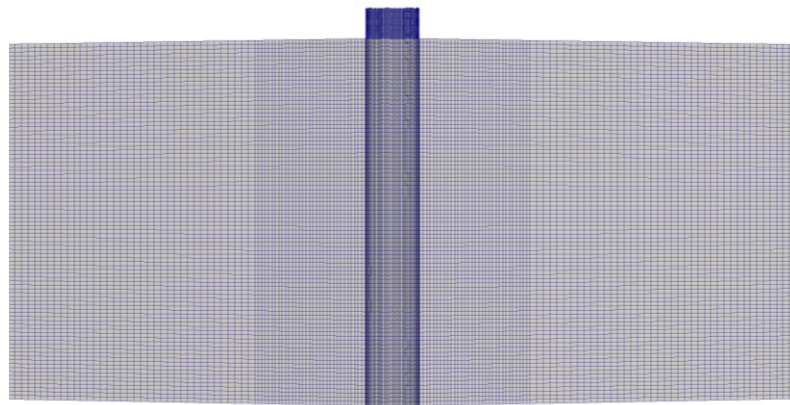**Figure 4.9: Velocity profile for impinging jet.**

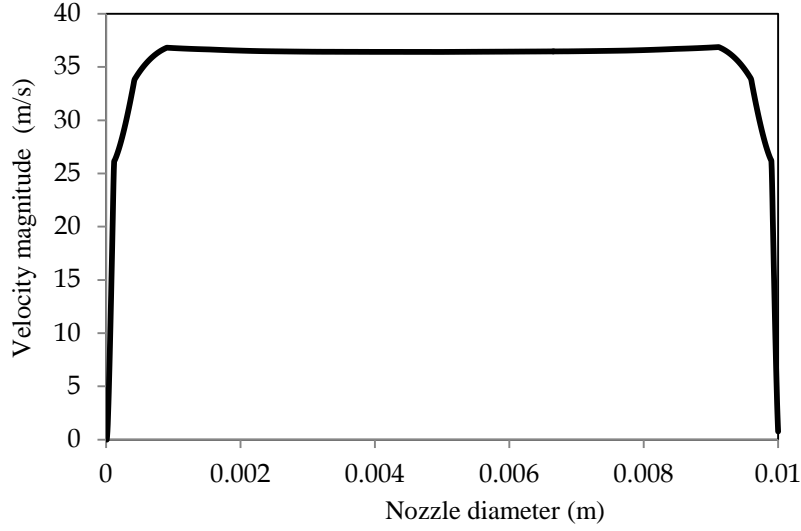**Figure 4.10: Mesh configuration used for simulating jet impingement.**

Figure 4.11: Velocity profile at the nozzle exit.

Zero gradient boundary condition is imposed on the wall and outlet boundaries except for the high Reynolds number Realizable $k - \epsilon$ model which requires imposing a wall function at the wall. Inlet values of $k, \epsilon \ and \ \omega$ are calculated from the following equations [11]:

$$k = \frac{1}{2}\left(u'^2 + v'^2 + w'^2\right) \qquad (4\text{-}2)$$

$$u' = v' = w' = IU_{inlet} \qquad (4\text{-}3)$$

$$\epsilon = \frac{c^{0.75}k^{1.5}}{l} \qquad (4\text{-}4)$$

$$l = 0.07L_c \qquad (4\text{-}5)$$

where

u', v', w', the velocity fluctuations in the directions x, y, z respectively.

I: the turbulence intensity

U_{inlet}: inlet velocity

$c = 0.09$, an empirical constant

l : the length scale

L_c : the characteristic length (nozzle diameter).

The initial conditions are as follows:

Pressure: 1 bar

Temperature: 300 K

Velocity: zero

Turbulence parameters (k, ϵ, ω): Initially, there is no turbulence (zero values).

Thermodynamic properties: Constant thermodynamic coefficients of air, with a specific heat capacity $c_p = 1000$ J/ (kg· K); Prandtl number $= 0.7$ and dynamic viscosity$= 1.8 \times 10^{-5}$Kg/ (m.s).

Time Step: Maximum Courant number was set to be 1.0 so time step is variable but it stabilizes around 2×10^{-6} s. Courant number, C, is defined in terms of velocity magnitude, u, time step, t and Δx length interval.

$$C = \frac{u\Delta t}{\Delta x} \qquad (4\text{-}6)$$

B. Solver evaluation

First, we evaluate *sonicFoam*. The state variables are time dependent, but the solution gets to quasi-steady state after around 0.015 sec of simulation time as shown in Figure 4.12. Therefore, all the observed variables are averaged over time (excluding the initial period of jet development). OpenFOAM has several Reynolds averaged Navier Stokes turbulence

models for compressible fluids. The following turbulence models has been tested: Shear Stress Transport $k - \omega$ model (SST) [18] Realizable $k - \epsilon$ Model [16], Launder & Sharma $k - \epsilon$ Model [15]. More details about these models are in subsection 2.2.

Figure 4.13 depicts the variation of the average velocity at the symmetry axis as the jet approaches the impingement plate. y/d is the height above plate. Average axial velocity, U , is normalized by bulk velocity (U_b). Bulk velocity is calculated according to the following equation [29]:

$$\frac{U_b}{U_{CL}} = 0.811 + 0.038(log(Re) - 4) \tag{4-7}$$

where U_b is the bulk velocity, U_{CL} is the centerline velocity, Re is the Reynolds number.

We note that the three models follow the general trend of the experimental data. SST $k - \omega$ model and Realizable $k - \epsilon$ perform better than Launder and Sharma $k - \epsilon$ model and give approximately the same results at *y/d* <0.5 and *y/d* >1.5. SST model gives better results than the other 2 models, especially in the region where: 1.4> *y/d* >0.5.
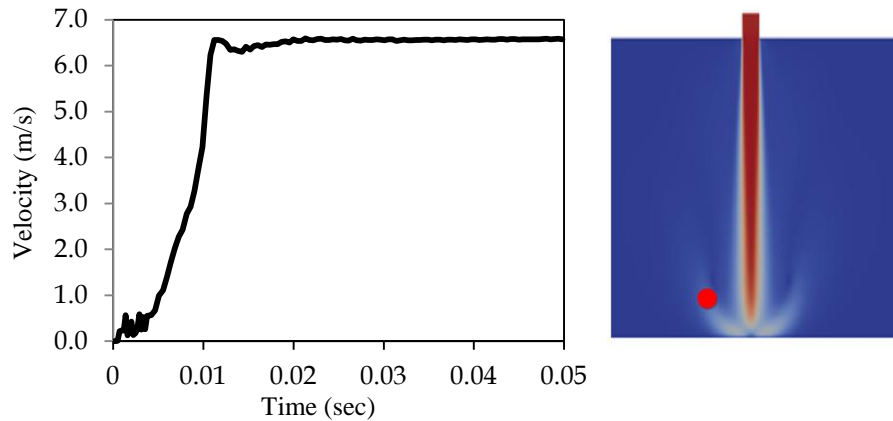

Figure 4.12: Velocity change with time at a point which is labeled (on the right).
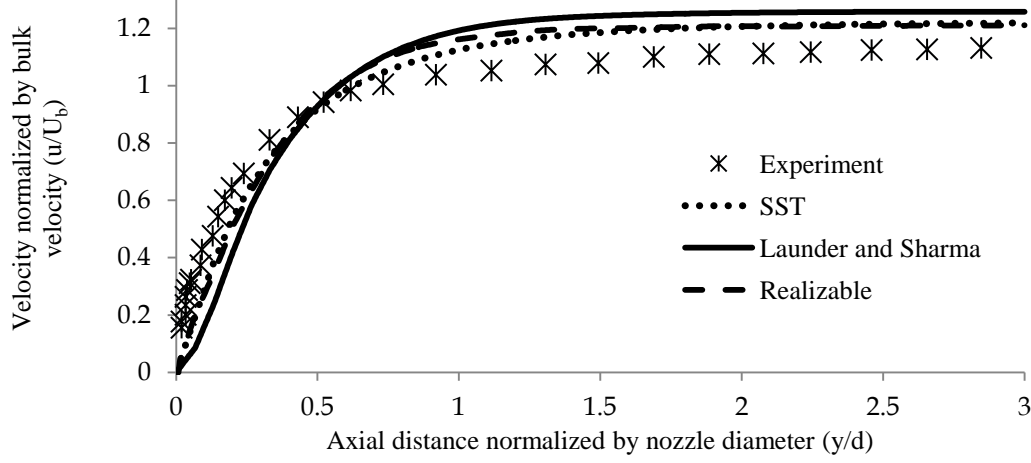
Figure 4.13: Mean velocity normal to the wall computed by SST, Launder and Sharma and realizable turbulence models.

The near-wall behavior is demonstrated in Figure 4.14 which shows the absolute values of the velocity very close to the wall. It is notable that the experimental mean velocity does not go to zero near the wall. In reference [29] this was attributed to the fact that when the mean velocity approaches zero, the measurement signal is more affected by the turbulent fluctuating velocity near the wall. Assuming that the velocity fluctuations, u', (radial and axial) are isotropic, velocity, U, was corrected to be U_c, in the same reference, by the equation:

$$U_c = \sqrt{U^2 - 2u'^2}$$

(4-8)

This correction reduces the mean velocity near the wall and negligibly influences the results far from the wall. In Figure 4.14, velocity calculations based on SST model come between the experimental velocity and the corrected velocity.

The Wall jet

The turbulent wall jet is the jet reflected by a wall and extends to the other side as it can be seen in Figure 4.9. The wall jet consists of two layers. The inner layer is similar to the boundary layer. The outer layer is like a free shear flow. Figure 4.15 is a diagram of the typical wall jet which is characterized by the jet half width, $y_{1/2}$, which is the location where $u_r/u_m = 0.5$. u_r is the radial velocity and u_m is the maximum radial velocity in wall jet.
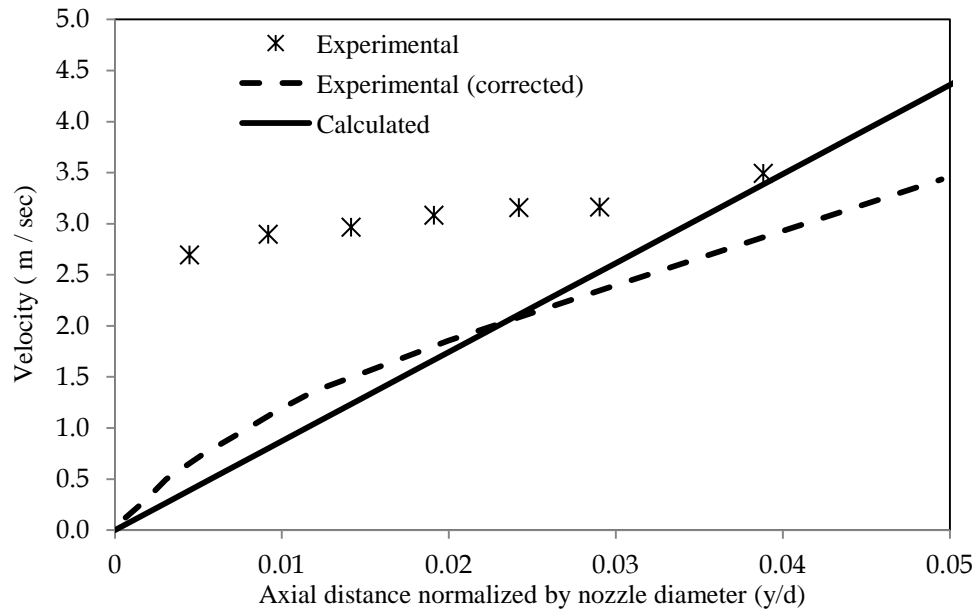

Figure 4.14: Near wall axial mean velocity.

To assess the CFD calculations for the turbulent wall jet growth and spreading, radial growth of jet half width computed with OpenFOAM is compared with experimental results in reference [29].

In Figure 4.16, the experimental radial wall jet grows linearly with radial distance. It is noted that both Low Reynolds Number turbulence models (SST and Launder and Sharma) capture (over-predict) the wall jet growth. Realizable $k - \epsilon$ turbulence model does not simulate the jet growth. Difference in wall jet growth between the calculations of the three turbulence models is shown in Figure 4.17.
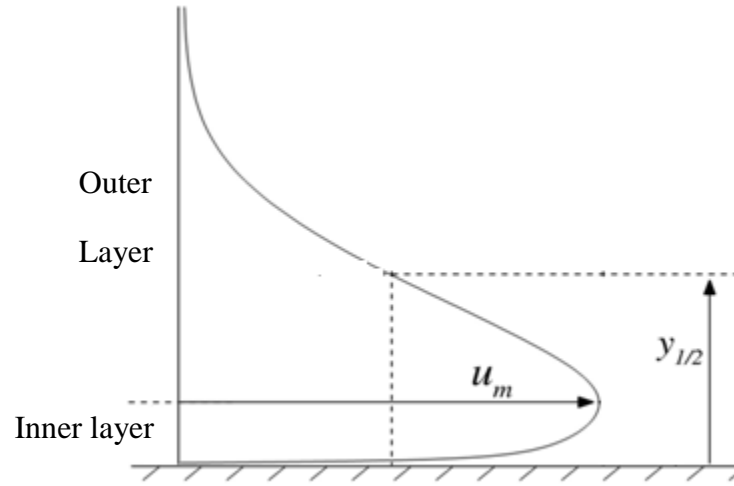
Figure 4.15: Fully developed velocity profile of a wall jet [30].
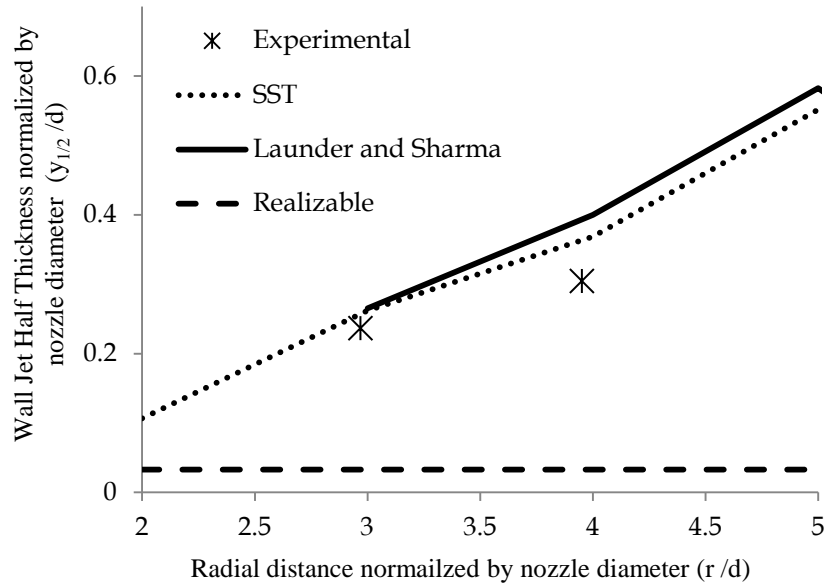
Figure 4.16: Radial Growth of jet half width.

Launder & Sharma $k - \epsilon$ Model   SST $k - \omega$ Model   Realizable $k - \epsilon$ Model
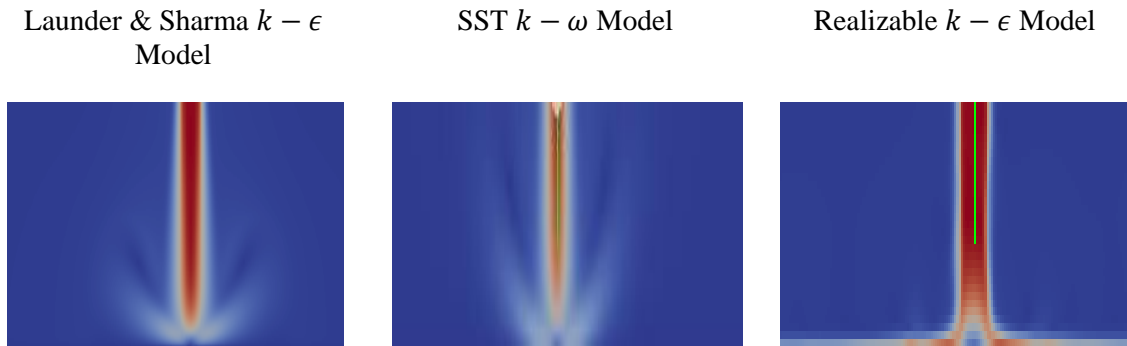

Figure 4.17: Radial wall jet as expected by different turbulence models.

Performance of different solvers

All the previous results were obtained with the pressure-based solver, *sonicFoam*. The next solver to be tested is the compressible density based solver, *rhoCentralFoam*. To stabilize the solver, we had to decrease the maximum Courant number from 1 to 0.25. This led to increasing the simulation cost by a factor of 83 times so *rhoCentralFoam* solver was deemed to be too computationally expensive for this case. The simulation cost of the third solver, *compressibleMultiphaseInterFoam*, is 2.5 times more expensive than *sonicFoam*.

Figure 4.18 shows the variation of the average velocity at the symmetry axis as jet approaches the impingement plate calculated by both *sonicFoam* and *compressibleMultiphaseInterFoam* (using the same mesh and boundary conditions). For both solvers, SST turbulence model is used and the maximum Courant number is 1.0. Both solvers give the same trend, but *sonicFoam* give better results with less expensive simulation. This includes both Courant number effect and slower performance per iteration. One has to keep in mind that the second solver also has the multiphase flow simulation capability which is relevant to the problem of interest in this work.

The near-wall behavior for the absolute values of the velocity very close to the wall as calculated by both solvers is shown in Figure 4.19. Both solvers give reasonable results. For the wall jet, Figure 4.20, none of the two solvers estimates the jet half width successfully.
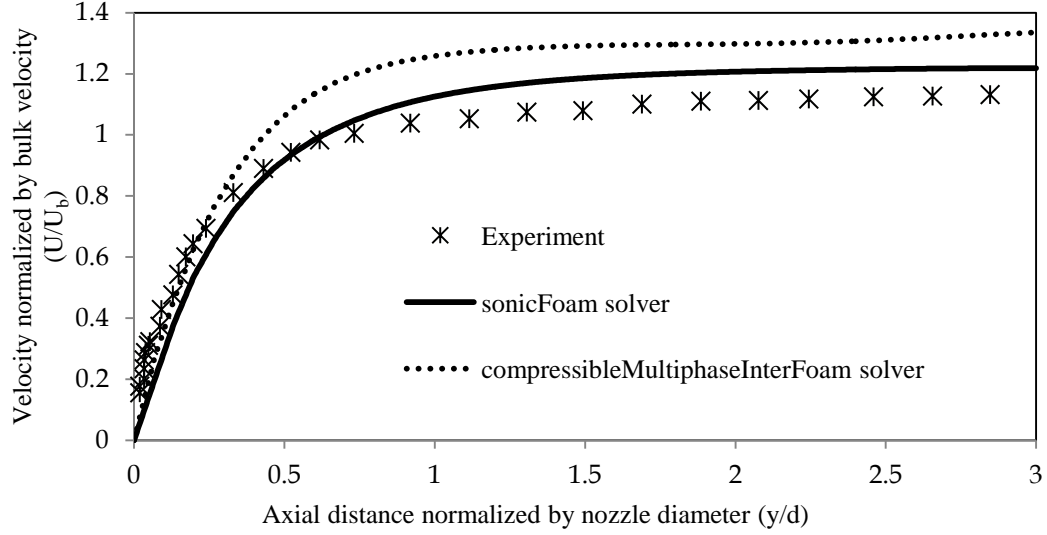
Figure 4.18: Mean velocity normal to the wall calculated by 2 solvers.

C. Comments and discussion

In this section we will summarize our observations based on the presented separate effect study.

Shear stress turbulence model predicts the jet impingement and wall jet behavior better than the other models and this agrees with what Zuckerman concluded in his review paper that SST model gives a good compromise between accuracy and simulation cost [12]. Both Low Reynolds number models captured the reflection of the jet from the wall (wall jet). This may attributed to the algebraic damping functions of these models that damp certain terms in the model so the behavior of the eddy viscosity near the wall is corrected.
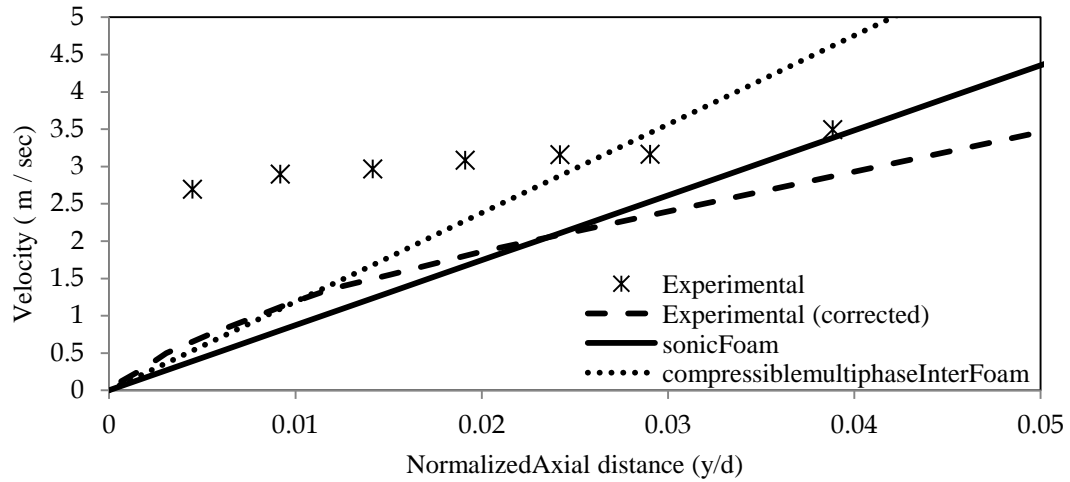
Figure 4.19: Near wall axial mean velocity as computed by two solvers.
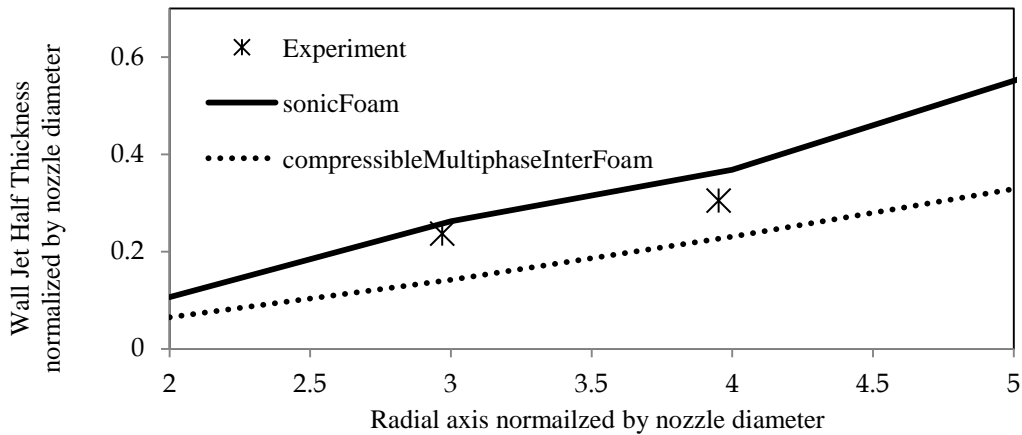
Figure 4.20: Radial Growth of jet half width computed by 2 solvers.

One of the choices for near wall treatment is using the wall functions. We noticed that wall functions lead to the absence of the wall jet. Wall functions which predict the flow properties in and above the viscous sub-layer are based on different geometries than jet impingement. Therefore, wall functions do not determine the near-wall velocity correctly, especially in

cases when the jet reflects from the target [12]. Impinging jet has different flow patterns with different physics (free jet, stagnation region, and wall jet) but usually any model is adjusted to succeed in simulating one specific pattern. The general solution for this issue may be using different models in different regions. Menter's Shear Stress Transport model is a kind of hybrid model because it combines the $k - \omega$ near the wall and the $k - \epsilon$ far from the wall [12].

Two equation turbulence models that are tested in our work assume the isotropy of Reynolds stresses so the turbulent production and dissipation is isotropic. For the stagnation region, this assumption is not true. Therefore, one of the suggestions, for future work, is using the anisotropic Reynolds Stress models which compute the Reynolds stress and discard the eddy viscosity method but these models are probably more expensive.

In an attempt to get better results, the total mesh size was increased twice, but that did not improve the results. Also, special refinement at the wall sub-layer ($y^+ < 5$) did not improve the results. Adaptive mesh refinement would be essential to simulate transient jet impingement.

Comparing the performance of different solvers, we note that *rhoCentralFoam* is the only density-based solver while the other solvers are pressure-based solvers. In general, velocity is obtained from the momentum equations. In the density based code, density is calculated from the continuity equation and the pressure is calculated from the equation of state. On the other side, for the pressure based solvers, pressure field is determined by the pressure equation which is gained by taking the divergence of the momentum equation and applying continuity equation. Therefore, the density based solver is not appropriate for this incompressible case because small errors in density may lead to large errors in calculating the pressure. This is

probably the reason that the solver needed to reduce the time step so much. Also, when comparing the performance of the solvers, we notice that *sonicFoam* is the only implicit solver while the other two solvers are explicit. For explicit solvers, errors are accumulated with each time step and usually explicit methods need smaller Courant number compared to implicit solvers. In fact, explicit solvers typically cannot converge at all if the Courant number is greater than 1. Therefore, *compressibleMultiphaseInterFoam* solver may achieve better results if the Courant number is reduced.

4.2.2 Under expanded sonic jet flow problem

The second validation experiment is the under-expanded sonic jet as described in [31] Subsection (A) gives a description of the problem and the problem setup. CFD capability is then evaluated by comparing numerical results to experimental data using different turbulence models and different OpenFOAM solvers in subsection (B). Conclusions and insights gained from the results are summarized in subsection (C)

A. Description

Under-expanded jet is the last phase in the progress of flow pattern through a nozzle connecting high pressure chamber and low pressure reservoir. Figure 4.21 shows the velocity profile of under-expanded jet as simulated by OpenFOAM. In Figure 4.21, Mach number is the ratio of speed of air relative to the local speed of sound. The jet inlet diameter, d, is 0.01m. The jet Reynolds number is 10^6 based on the jet sonic velocity, diameter and fluid viscosity. The distance from the jet nozzle to the impingement plate, H, is 40 nozzle diameters, $(H/d = 40)$. Jet centerline to outlet distance is $15d$. The simulation is done with non-uniform three dimensional meshes which are refined in the radial direction around the jet

and axial direction in the vicinity of the inlet, Figure 4.22. The adopted grid size for initial computations is 45 (radial) × 120 (normal to the plate).

The boundary conditions are as follows:

Pressure: Inlet total pressure is 5 bars while the outlet pressure is 1 bar so the ratio of exit total pressure to ambient pressure is around 5. Zero gradient condition is imposed on the walls.

Temperature: Temperature at the inlet and outlet is 300 K. Zero gradient condition is imposed on the walls.

Velocity: Inlet velocity is sonic velocity, 340 m/s. No slip (zero velocity) boundary condition is imposed at the walls. Boundary condition at the outlet is zero gradient.

Turbulence parameters (k, ϵ, ω): Turbulent inflow conditions were calculated based on low turbulence intensity, 0.05 similar to the first validation case. The initial conditions and thermodynamic properties are the same as the first validation experiment.

B. Solver evaluation

First, we evaluate *sonicFoam*. The state variables are time dependent, but the solution gets to a quasi-steady state after around 0.005 second as shown in Figure 4.23. Therefore, all the observed variables are averaged over time (excluding the initial period of jet development). Figure 4.24 depicts the jet centerline Mach number as measured experimentally and simulated by different mesh sizes. The local Mach number is computed by OpenFOAM with a utility called *Mach*. Local Mach number (M) for ideal gas is calculated based on the specific heat ratio (γ), inlet pressure, P_{inlet} and local pressure, P

$$M = \left[\frac{\gamma + 1}{2\gamma} \left(\frac{P_{inlet}}{P} - 1 \right) + 1 \right]^{1/2}$$
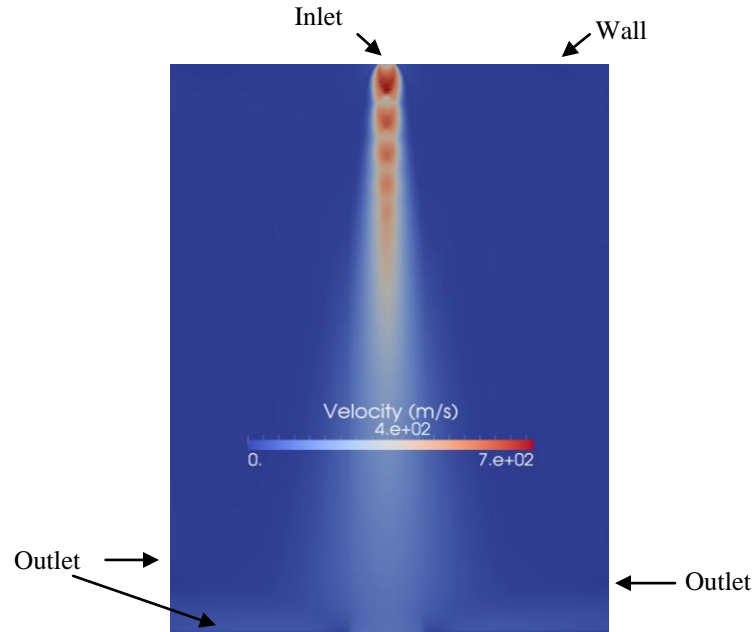
(4-9)

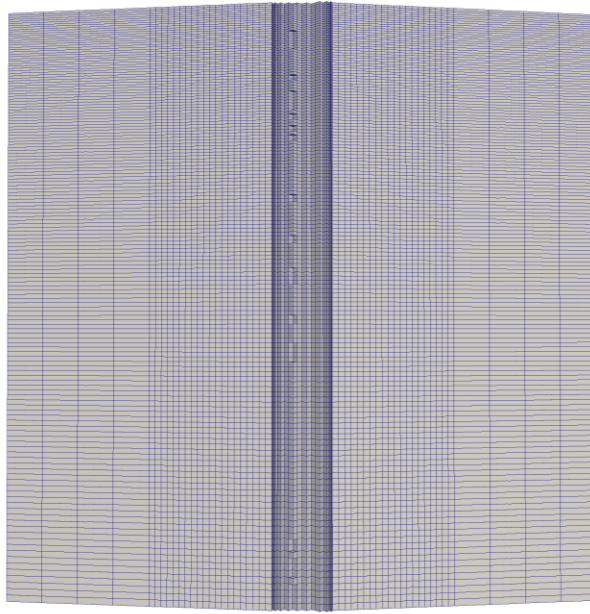**Figure 4.21: OpenFOAM Simulation of under-exapnded jet.**

Figure 4.22: Mesh configuration used for simulating under-expanded jet.

In Figure 4.24, computations over-estimate the Mach number, especially near the inlet. Simulation and experiment give the same Mach number downstream. Computations show 4 Mach number peaks compared to 7 peaks in the experimental data. Refining the grid in the axial direction gives sharper and stronger peaks, but Mach number is still overestimated near the inlet.
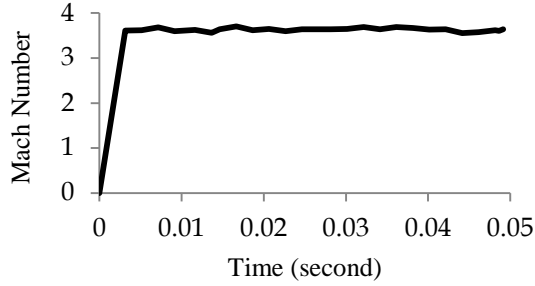
Figure 4.23: Mach number change with time at a point which is labeled in Figure 4.21. Performance of different solvers

All the previous results for this separate effect study were obtained with the pressure-based solver, *sonicFoam.* The next solver to be tested is the compressible density based solver, *rhoCentralFoam.* To stabilize the solver, we had to decrease the maximum Courant number from 1 to 0.3. However, this led to cheaper simulation (simulation cost is reduced by 50 %). For the third solver, *compressibleMultiphaseInterFoam,* the maximum Courant number was decreased down to 0.7 to stabilize the solver. The solver was not stable and the simulation cost increased 10 times relative to the density based solver, so *compressibleMultiphaseInterFoam* solver was deemed to be too computationally expensive in this case. Figure 4.25 shows the jet centerline Mach number calculated by calculated by both *sonicFoam* and *rhoCentralFoam* (using the same mesh and boundary conditions). For both solvers, SST turbulence model is used. *rhoCentralFoam* gives more peaks and achieves better results $at\ x/d > 10$ but the first Mach number peaks are much more overestimated compared to *sonicFoam.*
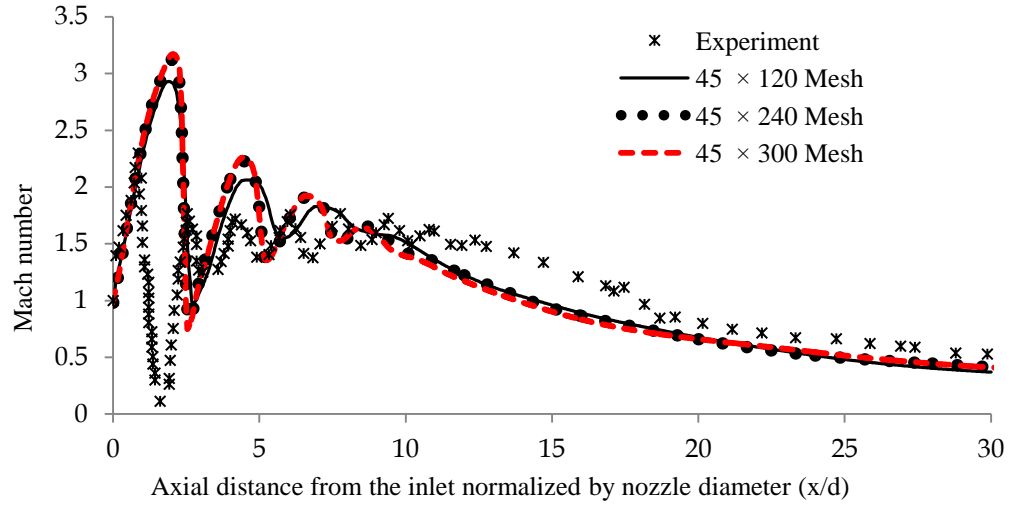
Figure 4.24: Jet centerline Mach number.

C. Comments and discussions

For this compressible flow, pressure is a function of density and hence density based solver performs resolution compared to pressure based solver with the same grid. Changing the turbulence model to Realizable $k - \varepsilon$ model did not improve the results. Mach number peaks (related to the formation of Mach disks) are thin, so probably more mesh refinement is needed to capture this peak. *CompressibleMultiphaseInterFoam* is an explicit pressure based solver. That's why it is not as appropriate as density based solver, *rhoCentralFoam* and more expensive than implicit solver, *sonicFoam.*
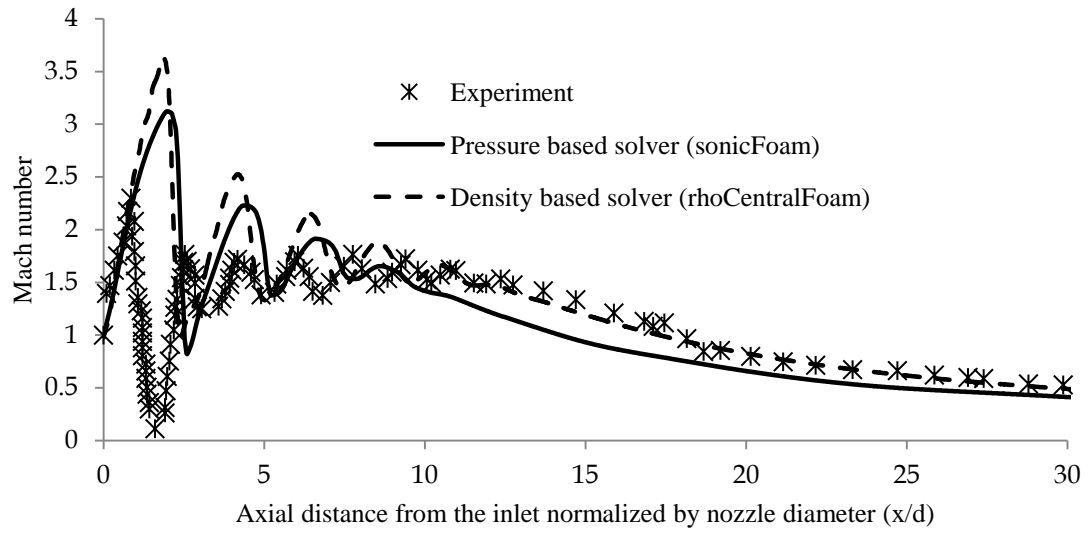
Figure 4.25: Jet centerline Mach number computed by two solvers.

5 Conclusions and future work

High-pressure blowdown flow from the RCS and containment's large-scale convective mixing present a formidable computational challenge. (It needed 1 week computing time on a 128-processors cluster to simulate 10 seconds of steam blowdown although the mesh is not necessarily fine enough). It would be much more expensive to simulate DCH scenario.

EMDAP process was adopted to assess CFD capability. PIRT was created based on phenomena observed in simulation. For future work, PIRT would help to determine which physics still need validation.

Low pressure and temperature regions of the jet might cause steam to condense (as discussed in 4.1.4.7). This phenomenon might affect steam momentum and subsequently mitigate energy transfer that governs the DCH potential.

Menter's SST model succeeded to capture the jet flow, jet impingement and wall jet because it is a hybrid model, which combines the $k - \omega$ formulation in the flow region near the wall and the $k - \epsilon$ formulation in regions far from the wall.

There is a critical need for developing turbulence models that are hybrid or adaptive so they can reflect evolving flow patterns. The success of this effort requires new experimental data. While deem-relevant experiments exist, they often are small-scale and separate-effect tests that were conducted without rigorous control. New validation-grade experiments combined with techniques for more effective use of available data are instrumental for calibration and validation of CFD models.

Pressure implicit based solver is the best among available options in OpenFOAM for simulation of steam blowdown, particularly in its capability for dealing with both compressible and incompressible flow.

EMDAP is a systematic and comprehensive process that requires significant efforts. This work is just at the beginning of implementing EMDAP. More work is needed in areas like scaling analysis. Also, more validation experiments with different degree of complexity may be required to assess the model adequacy.

In summary, a state-of-the-practice CFD solver like OpenFOAM can be used to simulate and study fluid dynamics phenomena in a nuclear reactor accident such as steam blowdown. The code can capture the major physics and without tuning of parameters obtained from experimental data like other simplified models. However, traditional fine mesh CFD is very expensive and thus there is a need to develop new so-called coarse-grained CFD methods. The future work will investigate a data-driven modeling of sub-grid scale turbulence that makes simulation flexible (adaptable to evolving flow patterns) and improvable (informed by new data) as well as affordable compared to traditional CFD.

6 References

1.   Seghal, B. R. ed., *Nuclear Safety in Light Water Reactors*, 1st ed. (Elsevier, 2012).

2.   Dorsselaere, J.-P. V., Albiol, T. & Micaelli, J.-C., *Research on Severe Accidents in Nuclear Power Plants, Nuclear Power - Operation, Safety and Environmen*, 1st ed. (InTech, 2011).

3.   Theofanous, T. G. & Dinh, T.-N., Integration of Multi-Phase Science and Technology with Risk Management in Nuclear Power Reactors: Application of the Risk-Oriented Accident Analysis Methodology to the Economic, Simplified Boiling Water Reactor Design. *Multiphase Science and Technology* **20** (2), 81-122 (2008).

4.   OpenFOAM User Guide: Chapter 1 Introduction, Available at http://www.openfoam.org/docs/user/userch1.php#x3-20001.

5.   Oberkampf, W. L., Verification and validation in computational fluid dynamics. *Progress in Aerospace Sciences* **38** (3), 209–272 (2002).

6.   Pilch, M., A Two-cell equilibrium model for predicting direct containment heating. *Nucl. Eng. Des* **164**, 61-94 (1996).

7.   MELCOR, Available at http://melcor.sandia.gov/.

8.   Gothic, Available at http://www.numerical.com/gothic.php.

9.   AFDM, A Transient Fluid Dynamics Code, Available at https://www.iket.kit.edu/english/406.php.

10.   Nichols, R. H., *Turbulence Models and Their Applications to complex flows* (University of Alabama, Birmingham).

11.   Pope, S. B., *Turbulent Flows.* (Cambridge University Press, Cambridge

UK, 2000).

12.   Zuckerman, N., Jet Impingement Heat Transfer: Physics, Correlations and Numerical Modeling. *Advances in Heat transfer* **39** (2009).

13.   Bakker, A., Lecture 9 - Kolmogorov's Theory Applied Computational Fluid Dynamics, Available at http://www.slideserve.com/kert/lecture-9-kolmogorov-s-theory-applied-computational-fluid-dynamics (2002).

14.   Launder, B. E. & Spalding, D. B., The numerical computation of turbulent flows. *Computer Methods in Applied Mechanics and Engineering* **3** (2), 269-289 (1974).

15.   Launder, B. E. & Sharma, B. I., Application of the Energy-Dissipation Model of Turbulence to the Calculation of Flow Near a Spinning Disc. *Letters in Heat and Mass Transfer* **1** (2), 131-138 (1974).

16.   Shih, T. H., A New k-epsilon Eddy-Viscosity Model for High Reynolds Number Turbulent Flows - Model Development and Validation. *Computers Fluids* **24** (3rd), 227-238 (1995).

17.   Wilcox, D. C., *Turbulence Modeling for CFD*, 2nd ed. (Anaheim: DCW Industries, 1998).

18.   Menter, F. R., Two-Equation Eddy-Viscosity Turbulence Models for Engineering Applications. *AIAA Journal* **32** (8), 1598-1605 (1994).

19.   Li, Y., Characteristic and computational Fluid Dynamic Modelling of High-Pressure Gas Jet Injection. *Transactions of the ASME* **126** (2004).

20.   Chang,C.W., Personal communication (July 2014).

21.   U.S. Nuclear Regulatory Commission (NRC), Transient and Accident Analysis Methods Regulatory Guide Report No. 1.203, 2005.

22.   GE-Hitachi, Status report 100 - Economic Simplified Boiling Water Reactor   (ESBWR),   Available   at

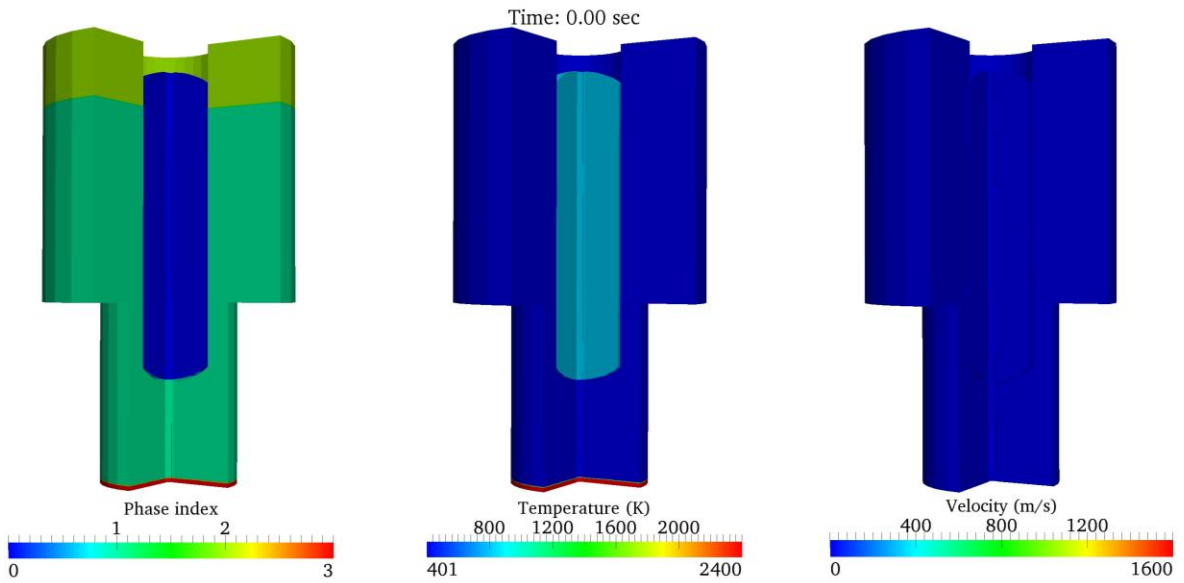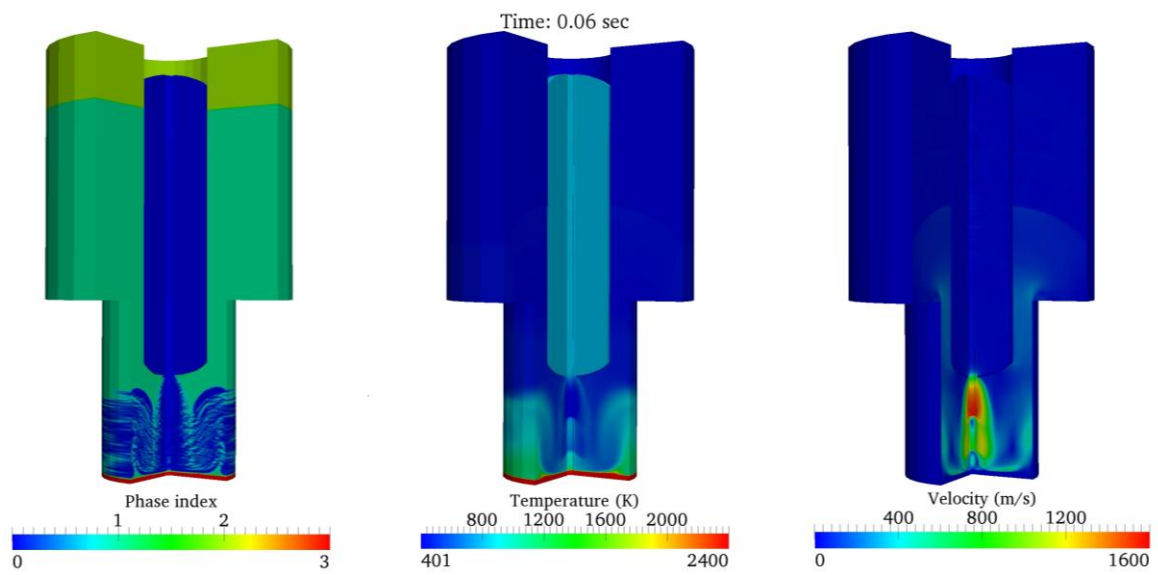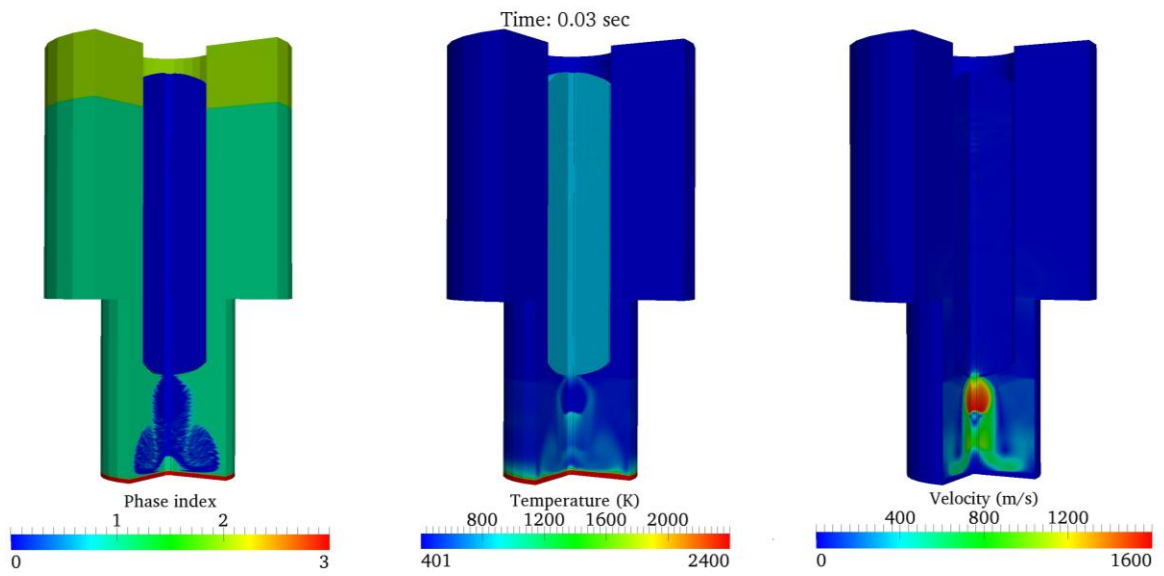https://aris.iaea.org/sites/.%5CPDF%5CESBWR.pdf (2011).

23.   D'Ambrosio, D., Physical and Numerical Experiments on an Under-Expanded Jet. *Meccanica* **34**, 267-280 (1999).

24.   Goldstein, R., Streamwise distribution of the recoverty factor and the local heat transfer coefficient to an impinging circular air jet. *Int. J. Heat Mass transfer* **29** (1986).

25.   Chung, Y. M., Numerical study of momentum and heat transfer in unsteady impinging jets. *Internation Journal of Heat and Fluid Flow* **23** (2002).

26.   Dauptain, A., Large Eddy Simulation of Stable Supersonic Jet Impinging on Flat Plate. *AIAA Journal* **48**, 2325-2338 (2010).

27.   Seydein, S. H., Modelling of a single confined turbulent slot jet impingement using various k-ϵ turbulence models. *Appl.Math.Modelling* **18** (1994).

28.   Khalil, I., The Structure of Suprecritical Fluid Free Jet Expansions. *AIChE Journal* **50** (1) (2004).

29.   Cooper, D., Impinging jet studies for turbukence model assessment-1. Flow-fields experiments. *Int. J. Heat Mass Transfer* **36**, 2675-2684 (1993).

30.   Ugo, P. & Banyassady, R., Department of Mechanical and Materials Engineering, Available at http://me.queensu.ca/People/Piomelli/Walljets.html (2013).

31.   Birkby.P & Page.G.J, Numerical predictions of turbulent underexpanded sonic jets using a pressure-based methodology. *Proc Instn Engrs* **215** (3), 165-173 (2001).
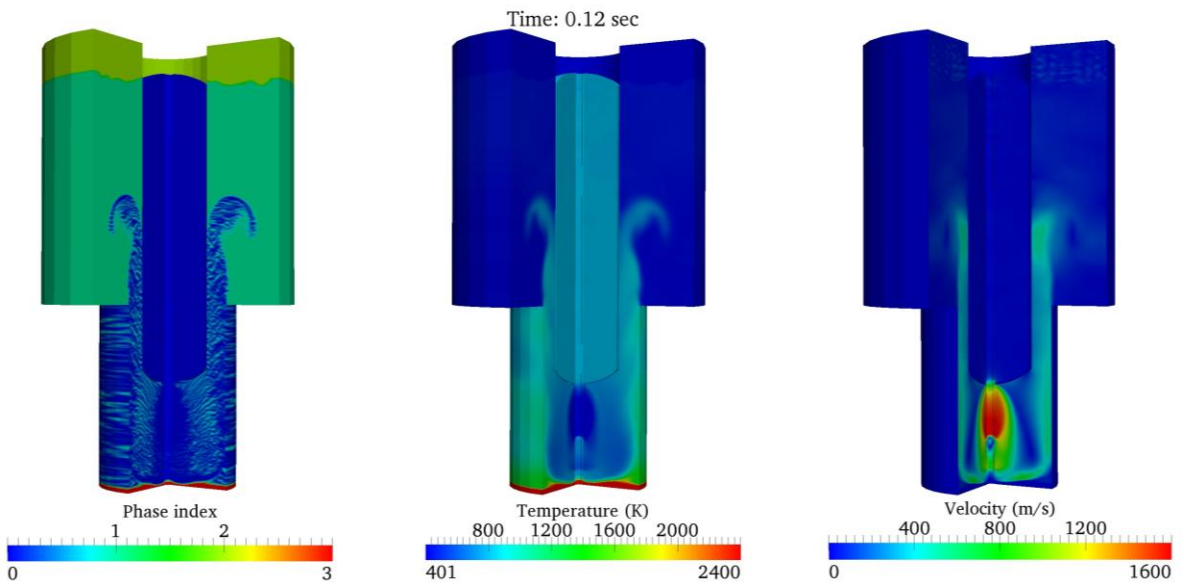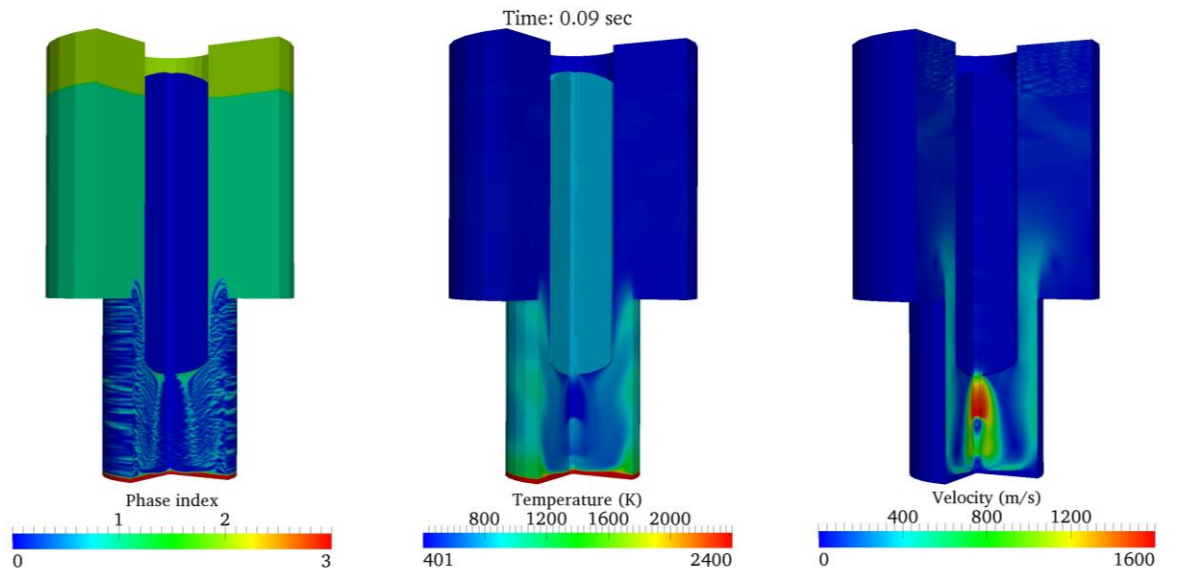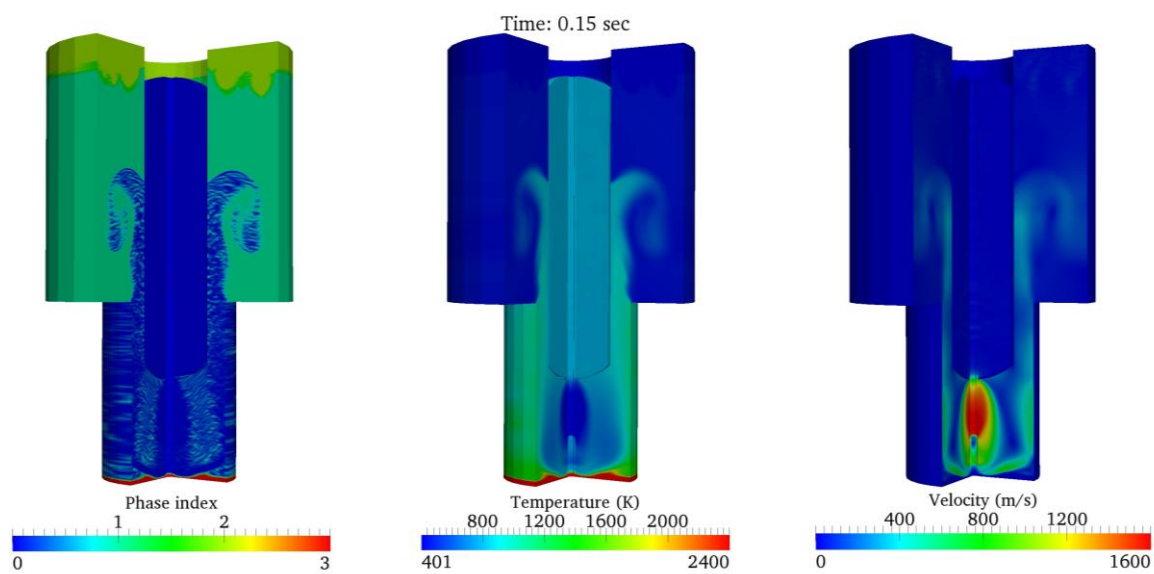
APPENDICES

Appendix A

In this appendix, snapshots of DCH-type simulation are presented. These snapshots show (from left to right) phase distribution, temperature and velocity. Numbers 0, 1, 2 and 3 in the phase index scale refer to steam, air, hydrogen and corium (melt) respectively. This simulation was based on idealization of one of the cases in [3]. System parameters are the same like Table 3.1. Hydrogen volume is 25% of UDW. The initial mass of corium in the lower drywell floor is 300 tons (equivalent to height of 38 cm).

Time: 0.03 sec

Phase index

Temperature (K)

Velocity (m/s)

Time: 0.06 sec

Phase index

Temperature (K)

Velocity (m/s)

Time: 0.09 sec

Phase index

Temperature (K)

Velocity (m/s)

Time: 0.12 sec

Phase index

Temperature (K)

Velocity (m/s)

Time: 0.15 sec

Phase index

Temperature (K)

Velocity (m/s)

Appendix B

In this appendix, snapshots of the steam blowdown simulation in the case, described in chapter 3, are presented. These snapshots show (from left to right) vertical velocity (in the z direction), pressure and temperature.

Time: 0.10 sec

Uz (m/s)

Pressure (pa)
1e+6

Temperature (K)

Time: 0.50 sec

Uz (m/s)

Pressure (pa)
1e+6

Temperature (K)

Time: 1.00 sec

Uz (m/s)

Pressure (pa)
1e+6

Temperature (K)

Time: 1.50 sec

Uz (m/s)

Pressure (pa)
1e+6

Temperature (K)